nature research

https://doi.org/10.1038/s41586-020-2970-9

Supplementary information

Unconventional ferroelectricity in moiré heterostructures

In the format provided by the authors and unedited

Supplemental Information
for
"Unconventional ferroelectricity in moiré heterostructures"

This file includes:

I. Note on first- and second-order moiré p.2

II. Discussion on possible alternative origins of resistance switching

II.1. Discussion on extrinsic charge trapping states p.3

II.2. Discussion on lattice symmetry and lattice driven ferroelectricity p.4

II.3. Discussion on moiré lattice reconstruction and domain walls p.6

III. A possible microscopic picture - interlayer charge transfer p.7

IV. Band structure calculations p.13

V. Additional data and analyses

V.1. Device H1

V.1.1 Resistance switching behavior at zero B field p.18

V.2. Device H2

V.2.1 Resistance switching behavior at zero B field p.19

V.2.2 Additional capacitance data p.22

V.2.3 Magnetic field dependent measurements p.23

V.3. Device H4

V.3.1 Resistance switching behavior at zero B field p.24

V.3.2 Transport simulations based on a phenomenological model p.28

V.4. Additional Devices p.30

VI. References p.31

I. Note on first- and second-order moiré

In the main text, we mentioned that bilayer graphene and BN form a long wavelength moiré pattern at zero-degrees twist angle due to their lattice mismatch. Here, we hope to discuss the scenario of 30-degrees twist angle alignment and explore the concept of first- and second-order moiré.

We start from a generic discussion of stacking between two honeycomb lattices as shown in Fig. S1. δ is the lattice mismatch and θ is the alignment angle. As shown in Figs. S1**a,b**, at $\theta = 0°$, a long wavelength moiré pattern is more significant when the lattice mismatch δ is small. By contrast, at $\theta = 30°$ (see Figs. S1**c,d**), a long wavelength moiré pattern is more significant when the lattice mismatch δ is large.

In the case of graphene and BN, the lattice mismatch is small ($\sim 1.8\%$). This small number refers to the mismatch between a single graphene unit cell and a single BN unit cell. However, because of lattice periodicity, one can also consider the mismatch between M unit cells of graphene and N unit cells of BN. Indeed, we found a large mismatch of $\delta \sim 15\%$ between a 15×15 graphene supercell and a 17×17 BN supercell (Figs. S1**e**), which leads to a moiré pattern with periodicity of 7.5 nm at $\theta = 30°$. Because the large mismatch is achieved by supercells from each layer, this moiré pattern is also referred as the second-order moiré pattern. Interestingly, we only find a long-wavelength second-order moiré pattern at $\theta = 30°$, but not at $\theta = 0°$ and $\theta = 20°$.

Therefore, in devices where the BLG is aligned with one BN flake at $\theta \sim 0°$ and with the other BN flake at $\theta \sim 30°$ (*e.g.*, Device H2), we expect the BLG to form a first-order long-range moiré pattern with one BN flake and a second-order long-range moiré pattern with the other BN flake. Noticeably, these two moirés have similar wavelengths. In terms of the electronic band structure, although the effect of second-order moiré pattern is not extensively studied, we in general expect it to create band folding and moiré sub-bands in a similar but potentially weaker fashion as the first-order moiré.

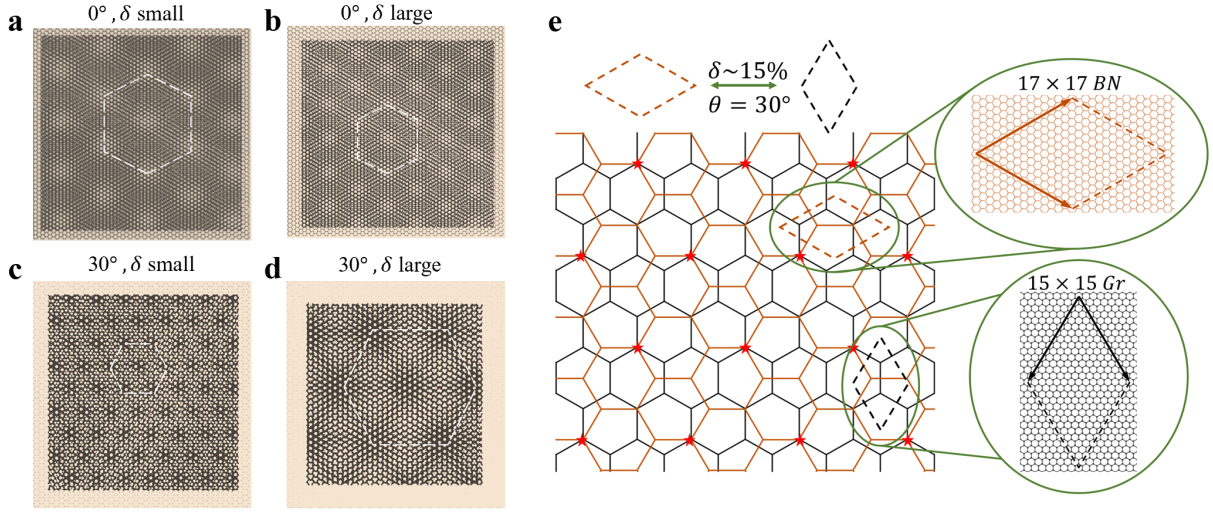

Figure S1: **a-d,** Schematics of moiré patterns at 0° and 30° for small and large lattice mismatch δ. **e,** Schematics of a second-order moiré pattern formed between a 15×15 graphene supercell and a 17×17 BN supercell.

II. Discussion on possible alternative origins of resistance switching

II.1. Discussion on extrinsic charge trapping states

In the main text, we briefly discussed the relevance of extrinsic charge trapping states. In this section, we will elaborate on this. We consider two possible locations for the trapping states: (a) inside the BN dielectric; (b) at the moiré interface between BN and graphene. We first discuss scenario (a) with the following "control experiments":

Control devices with BN as dielectric:

1. We, as well as many other groups, use BN as a dielectric for most of our 2D devices, including monolayer, bilayer, and trilayer graphene, WSe_2, WTe_2, and many others. The prominent hysteresis and "anomalous screening" features, particularly as in Devices H2 and H4 have not been observed before in such structures.

2. Normal BN-sandwiched bilayer graphene (not aligned) has been extensively studied for more than 10 years. We also measured such normal bilayer devices in this work. It is clear that such systems do not show hysteretic, particularly the "anomalous screening" features.

Considering the above experimental facts, it is unlikely that defects within BN can cause the prominent switching behavior in this work. The same argument can be also applied to a BN/graphene interface where the two layers are not closely aligned. What makes the configuration in our study more special is that we add the moiré potential into the system by aligning the bilayer graphene with the BN. Therefore, we consider impurity states unique to the moiré interface, for example, due to local lattice reconstruction [1]. Those impurity states can serve as charge trapping sites. Below, we discuss whether the LSAS behavior can be a result of the charge trapping states associated with the moiré interface.

Control moiré devices:

1. **Others' devices: monolayer graphene/BN moiré (one-side or both-side aligned with BN), twisted bilayer graphene/BN moiré, etc.** We note that recent experiments have studied a number of graphene/BN moiré systems, including monolayer graphene/BN moiré (one side or both sides aligned with BN) [2], twisted bilayer graphene/BN moiré [3], etc. However, the strong hysteresis with displacement field and LSAS have not been observed in any of these systems.

2. **Our devices made in this work: ABA trilayer/BN moiré, monolayer graphene/BN moiré:** We have fabricated an ABA trilayer graphene/BN one-side aligned device and a monolayer graphene double-aligned device. The dual-gated maps are shown in Extended Data Fig.1. Neither of them shows any hysteresis.

In the following, we also show how other experimental aspects can help us address the impurity scenario.

Scan rate of the displacement field: One important observation with defect/impurity induced charge trapping is that the resulting hysteresis strongly depends on the scan rate of the gate voltages. In Fig. S2 and Fig. S3, we compare the scan rate dependence between extrinsic charge trapping induced hysteresis, as observed in Ref. [4] and the rate-independent hysteresis observed in our samples. The schematics in Fig. S2 shows the hysteresis in an electrolyte-gated graphene device, where the hysteresis could be reduced by slowing down the gate sweeping rate due to the competing mechanisms of charge transfer from/to graphene and the capacitive gating effect. Therefore, the hysteresis shows an strong dependence on the different scan rates.

By contrast, our measurements show that the observed hysteresis is independent of the scan rate. In Fig. S3, we show the line traces (forward and backward) scanned along the displacement field direction at a fixed carrier density for scan rates comparable to those shown in Ref. [4]. It is clear that the hysteretic behavior is independent of the scan rate in terms of both the peak position and magnitude.

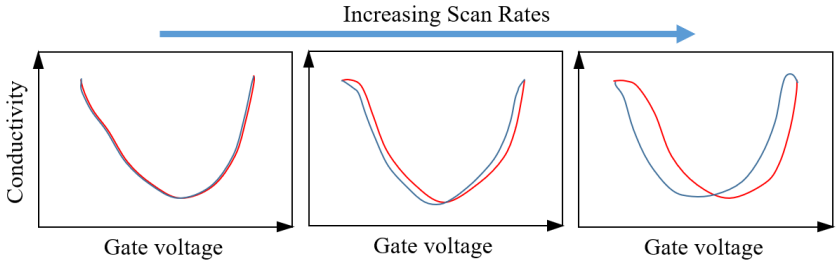

Figure S2: **Schematics of charge-trapping hysteresis.** The schematics from left to right illustrate the hysteresis in an electrolyte-gated graphene device with increasing scan rates. For the actual experimental data, please refer to Ref. [4].

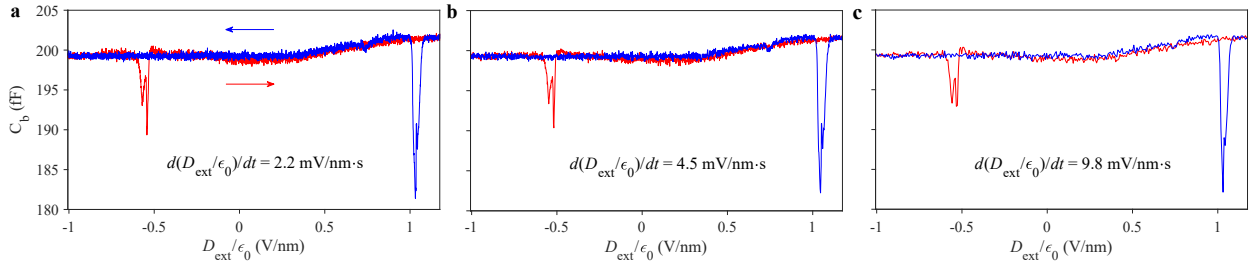

Figure S3: **Independence of hysteretic behavior of our devices on the scan rate . a-c,** Forward (red) and backward (blue) scans of the bottom capacitance, C_b, for different scan rates from Device H2 at a fixed nominal carrier density. Scan rates shown in each panel denote the rate at which the external displacement field $D_{\text{ext}}/\epsilon_0$ was changing in the BN dielectric layers. No systematic variation was observed in the capacitance features for a large range of scan rates from 2.2 mV/nm·s to 9.8 mV/nm·s.

II.2. Discussion on lattice symmetry and lattice driven ferroelectricity

In this section, we only consider the bilayer graphene/BN heterostructures without lattice reconstruction and domain walls. Lattice reconstruction and domain walls will be discussed in the next section.

Ferroelectric materials have an internal spontaneous electric polarization, which can be switched by applying an external displacement field. In conventional ferroelectric materials, the formation of such a dipole can be naturally understood as the spatial separation of the positive charge center (cation) and negative charge center (anion) within a unit cell. A small lattice movement can switch the electric dipole from one direction to the opposite direction, which corresponds to the two stable lattice configurations (local energy minima). For example, the recently discovered 2D ferroelectricity in bilayer WTe_2 [5] can be understood with such a picture. This mechanism can be regarded as lattice driven ferroelectricity. However, we find it unlikely that such a picture is relevant to our bilayer graphene/BN moiré system based on our experimental results and analyses. Our arguments are as follows:

Lattice model and its symmetry:

In the case of lattice driven ferroelectricity, there should be two equivalent energetically favorable lattice configurations that correspond to the two polarization states. Normal bilayer graphene (not aligned) has been studied very extensively over the past decade and the Bernal stacking is very stable. The Bernal-stacked bilayer graphene has inversion symmetry and cannot be polar. Moreover, no ferroelectric instability or spontaneous layer symmetry breaking has been found in normal bilayer graphene without a magnetic field.

We now consider bilayer graphene crystallographically aligned with the bottom BN. As we will show in the following, although locally the lattice stacking can correspond to polarization up or down, globally such polarization is averaged out by the moiré pattern.

Let's consider the case of perfect alignment between bilayer graphene and BN. In this case, we still have a translational degree of freedom between graphene and BN, *i.e.*, locally, how the boron and nitrogen atoms in BN are vertically aligned with carbon atoms in graphene. Because the low energy quadratic band touching arises from the A_b and B_t ("b"("t") refers to the bottom(top) layer) orbitals (Fig. S4), the problem boils down to how the boron and nitrogen atoms from the bottom BN affect the electrostatic potential of the A_b site. Following this argument, there are three distinct local lattice alignments:

1. The A_b site is vertically aligned with a boron site (cation) (Fig. S4**a**). In this case, the electrostatic potential (for electrons) at A_b decreases. Given that the potential at B_t is unaffected, this corresponds to an electrical polarization pointing up.

2. The A_b site is vertically aligned with a nitrogen site (anion) (Fig. S4**c**). In this case, the electrostatic potential (for electrons) at A_b increases. Given that the potential at B_t is unaffected, this corresponds to an electrical polarization pointing down.

3. The A_b site is vertically aligned with an empty site (Fig. S4**b**). In this case, the electrostatic potential (for electrons) at A_b roughly remains the same. Given that the potential at B_t is unaffected, this corresponds to a nearly zero electrical polarization.

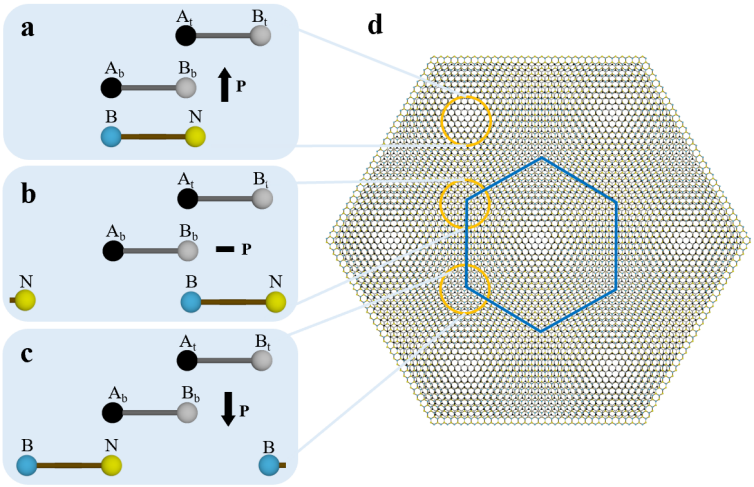

Figure S4: Drawing of the moiré pattern formed by bilayer graphene and bottom BN (with enhanced lattice mismatch for illustration purpose) and the side views of three different alignment configurations that correspond to upward, downward, and zero polarization.

Therefore, the three lattice alignments described above have realized P up, P down, as well as P zero. However, we have only considered local lattice alignments in the above analyses. When we look at the large scale, regions with different local polarization directions are distributed periodically across the moiré pattern, meaning that the potential provided by the boron nitride oscillates across the superlattice unit cell, leading to the cancellation of polarization upon spatial average. Indeed, our calculations (Fig. S10 in Section IV) show that the normal state electronic structure of a bilayer graphene/BN superlattice is always gapless, which is the signature of layer degeneracy or A_b and B_t orbital degeneracy. The lateral translation between graphene and BN will not change the band structure. This argument can be easily generalized to the case of bilayer graphene aligned with BN on both sides as well as the case of a small twist angle between the bilayer graphene and BN.

We note that the above argument can also be applied to the monolayer graphene/BN moiré system. Specifically, one would expect that the monolayer graphene remains gapless even in the presence of the moiré superlattice potential provided by BN, because of the cancellation due to average within the superlattice unit cell. On the other hand, experimental studies [2, 6] have shown the existence of a gap in the monolayer graphene/BN moiré system. The origin of this gap, however, remains to be fully understood. Theoretical studies have proposed different possibilities including electronic interactions [7] and structural reconstruction on the moiré scale [8].

Below, we discuss possible structural reconstruction in moiré lattices.

II.3. Discussion on moiré lattice reconstruction and domain walls

We have also considered the possibility of lattice reconstruction and domain walls. First, we enumerate a few facts that do not directly make use of our data.

1. A recent piezoresponse force microscopy (PFM) experiment on twisted bilayer graphene and other moiré lattices shows that a strain gradient present near the domain walls of moiré superlattices can produce a local electric polarization [1]. However, in that case, the direction of the strain gradient in these systems is considered to be fixed during lattice reconstruction and cannot be flipped with the external displacement field.

2. Moreover, domain walls and strain are usually non-uniform. By contrast, our features in our transport and capacitance data are very sharp, suggesting that they arise from the uniform response from the entire sample.

We summarize here our findings which are relevant to this discussion

1. **"Anomalous screening", LSAS:** In a conventional ferroelectric material, positive and negative bound charges move under the influence of the external displacement field, flipping the polarization. In this process, charges only move within the ferroelectric material. Therefore, the number of total mobile carriers does not change. This is the case for all well-studied ferroelectric materials (insulators with zero carrier density before and after the switching). This is also the case for the recently discovered ferroelectric metal few-layer WTe_2, which is a metallic system whose total mobile carrier density remains unchanged before and after the switching via displacement field [5]. In sharp contrast, because of the LSAS behavior in our system, the displacement field can change the total mobile carrier number of the bilayer graphene, as demonstrated by the Hall measurements. This anomalous behavior cannot be understood in the framework of conventional ferroelectric switching.

2. **Sharpness of the features in resistance and capacitance data:** The sharpness of the resistance peaks and the consistency over many consecutive scans demonstrate that the ferroelectric switching is a coherent response from the entire sample, rather than from local domain wall motions.

3. **Multiple transitions:** In Device H2, we are able to resolve multiple "anomalous screening" regimes. For example, in Fig. S18**c** and Extended data Figs. 7**a-b** as in the main text, we clearly see multiple different regimes where the resistance peaks run parallel to the top gate axis. Between adjacent regimes, the resistance peak is along a diagonal line as in the common scenario when both gates are working normally.

4. **Magnetic field effect of the electrical hysteresis:** Although the effect due to the magnetic field is beyond the scope of the current paper, we show the n-D maps under different magnetic fields, measured from Device H2 (Fig. S24). We see from **c-f** that under magnetic field, an additional switching of the resistance occurs near $D_{\text{ext}} = 0$. At the same time, the resistance at $+D$ and $-D$ becomes extremely asymmetric. These interesting observations suggest that the observed ferroelectricity is more likely to arise from electrons rather than lattice (which usually does not couple to the magnetic field directly).

Given the discussion in the above two sections, it remains to be seen whether the ferroelectricity and LSAS behavior observed can be reconciled with a model based on lattice structural changes. On the other hand, bilayer graphene has been predicted to exhibit various types of electronic order [9–12], including ferroelectric order [10], and experimental evidence for correlated behavior in pristine bilayer graphene has been reported [13–18] especially at high magnetic fields. Inspired by these facts, we suggest a microscopic theoretical picture based on spontaneous interlayer charge transfer driven by on-site Coulomb repulsion.

III. A possible microscopic picture - interlayer charge transfer

In this section, we provide a microscopic theoretical picture based on interlayer charge transfer. This picture could capture dominant features in our data. However, we do wish to caution that the main purpose of this picture is to help readers to better understand our data. At this point, existing experimental evidence is insufficient for us to unambiguously determine the microscopic mechanism. For instance, the band structure is unknown due to the absence of spectroscopic measurements. We hope that our discussion here can inspire future experimental and theoretical investigations. We focus on a specific picture accounting for the behavior of Device H4.

We focus on the following dominant features:

• When scanning away from the gapless point, the peak line becomes parallel to the V_{BG} axis upon reaching D_1 or D_2, depending on the scanning direction.
• As soon as the scanning sequence is reversed, both top and back gate appear to function normally.
• D_1 and D_2 are defined with respect to the gapless point.
• The hysteresis due to the "anomalous screening" behavior can result in a spontaneous polarization even when the external displacement field is removed.

We now describe our picture step by step:

Evolution of single particle band structure in bilayer graphene moiré system: As mentioned in the main text, normal bilayer graphene without an external displacement field has layer degeneracy with parabolic band touching, meaning that the electron wavefunction occupies the two layers with equal probability (Fig. S5**a**). In other words, layer polarization is zero everywhere. When an external displacement field is applied, the inversion symmetry is broken and a bandgap opens up. At the same time, a layer polarization is induced for states near the edges of the band gap.

To be concrete, let us consider the scenario of a positive displacement field in the +z direction. In this case, the top of the valence band will become "bottom layer" polarized (*i.e.*, the electron wavefunction at the edge of the valence band mainly occupies the bottom layer), whereas the electron wavefunction at the edge of the conduction band mainly occupies the top layer (Fig. S5**b**). Although the layer polarization increases with the external displacement field, the polarization is only concentrated at states near K/K' point of the Brillouin zone within a reasonable displacement field range.

In a bilayer graphene moiré system, the inclusion of a moiré potential introduces a large real space periodicity (L_{m}), which in turn leads to a small wavevector in momentum space ($k_{\mathrm{m}} \sim \frac{\pi}{L_{\mathrm{m}}}$) that defines the moiré superlattice Brillouin zone (BZ). Because the moiré wavevector (and thus the superlattice BZ area) is much smaller than the original BZ, it is conceivable that the entire moiré valence or conduction band become nearly fully layer polarized within the displacement field used in the experiments (Fig. S5**c**).

In real space, this means that electrons occupying the moiré valence or conduction bands are located on the bottom and top layer respectively in the case of a positive displacement field. In momentum space, the moiré valence and conduction bands become increasingly flat. The above describes the evolution of the single particle band structure without considering the effects of correlations.

Layer asymmetry and particle-hole asymmetry: A strong layer asymmetry is expected in our system based on experimental observation. In Devices H2 and H4, the LSAS behavior only appears on the top and bottom gate, respectively. Theoretically, layer asymmetry is the central condition to explain why LSAS behavior only appears on a particular gate, following the explanations below.

A necessary consequence of layer asymmetry is the particle-hole asymmetry and whether the valence band or conduction band shows a narrower bandwidth depends on the sign of the displacement field. Physically, the different moiré potentials experienced by the A_b and B_t atoms in bilayer graphene lead to particle-hole asymmetry. In bilayer graphene, the low energy electronic states near the charge neutrality are composed of the orbitals from the A_b and B_t atoms. With a finite displacement field, electronic states from the VB and CB localize on separate layers.

We first take Device H4 as an example. In Device H4, the device shows an anomalous response to the bottom gate in the LSAS regime. It is natural to assume that the correlation effect (due to the moiré potential) considered in our model is more significant for the electronic states associated with the bottom layer of bilayer graphene. In normal bilayer graphene, under a positive electric field, the valence band will pick up bottom-layer character. This is true for moiré bands as well. Because of the earlier assumption that the correlation effect is more significant for electronic states associated with the bottom layer, we consider

the situation where the moiré valence band becomes nearly flat (or more precisely, flatter than the moiré conduction band) upon applying an electric field. Consequently, it is the moiré valence band, rather than the conduction band, that opens up a Hubbard gap in our model. Similarly, in Device H2, only the top gate shows LSAS, which suggests that the top moiré potential (between the top BN and the top graphene layer) leads to stronger correlation effects compared with the bottom one. Noticeably, this layer asymmetry directly translates into the asymmetry between moiré conduction and valence bands in our case, leading to significant particle-hole asymmetry in our system.

In fact, this particle-hole asymmetry in moiré bands are already observed in various moiré graphene superlattice systems. Here, we refer to three systems: ABC trilayer graphene/BN moiré superlattice [19–21], Twisted double bilayer graphene [22–25], Twisted mono-bi moiré graphene [26–28]. In all these studies, the particle-hole asymmetry shows up not only near the charge neutrality, but also reflects as the absence of correlated quarter/half filling states on one side of the spectrum. A common feature between these systems and our bilayer graphene/BN moiré system lies in the layer degree of freedom. When low energy moiré bands couple to the layer degree of freedom, layer asymmetry can result in a particle-hole asymmetry. Therefore, even if the native band structure of each individual component is roughly symmetric at low energy, a particle-hole symmetry is not necessarily guaranteed in the presence of moiré superlattices.

Interlayer charge transfer and spontaneous polarization: As mentioned above, with a large enough positive displacement field, the topmost moiré valence band can become almost fully bottom layer polarized. The relatively flat band and the large layer polarization significantly enhances the on-site Coulomb repulsion. Based on our data, we assume that the on-site repulsion within the bottom layer (the moiré valence band in this particular discussion) is important.

There may exist a critical displacement field above which the on-site repulsion U in the bottom layer (valence band) is sufficiently strong that the moiré valence band splits into lower and upper Hubbard bands (Fig. S5**d**), the latter at an energy above the bottom of the moiré conduction band. An equivalent way of looking at this is that electrons will be spontaneously transferred from the valence band (bottom layer) to the conduction band (top layer), *i.e.*, an interlayer charge transfer occurs (Fig. S5**d**).

This process is actually in the opposite direction of the externally applied positive displacement field, inducing a spontaneous polarization.

D_1 and D_2: D_1 and D_2 can be understood as the displacement field at which the ($U > \Delta$) condition is achieved and therefore the interlayer charge transfer occurs. It is important to note that what determines the condition here is the interlayer displacement field "felt" by the low energy electrons of the bilayer graphene, namely the topmost moiré valence band and the bottommost moiré conduction band that we consider here. This is a result of a combined effect of the external displacement field and the spontaneous polarization of the bilayer graphene.

"Anomalous screening" phenomenon and its uni-directional nature: We can now try to understand the "anomalous screening" within the charge transfer picture. Let us assume that the bottom gate dopes carriers into the bottom layer, whereas the top gate dopes carriers into the top layer. When the charge transfer occurs, as one further increases the displacement field (*i.e.*, increases V_{BG}), the back gate is trying to add electrons to the fully polarized upper Hubbard band. However, this process is energetically unfavorable due to the large energy barrier of U that it needs to overcome. On the other hand, the top gate can work normally because of the absence of the Coulomb gap associated with the conduction band. Moreover, we can also explain the uni-directional nature of the "anomalous screening" phenomenon. A unique feature of the Mott physics is that even though the unfavorable double occupancy condition prevents adding more electrons into the system, taking an electron out of the bottom layer does not require extra energy and is favored. Therefore, when the displacement field scanning direction is reversed (*i.e.*, decreasing V_{BG}), the back gate is trying to remove electrons from the bottom layer, which is allowed. Hence, both top and back gate function as normal, and the normal bilayer graphene behavior is recovered.

The above discussion is focused on the positive displacement field case, but the argument for the negative displacement field towards D_2 is similar. In this case, the valence and conduction bands are localized on the top and bottom layers respectively.

Microscopically, based on our theoretical picture, we propose that the LSAS behavior should continue until all charges in the upper Hubbard band are transferred into the conduction band. Specifically, the LSAS (i.e., the interlayer charge transfer regime) starts when the top of the upper Hubbard band aligns with the bottom of the conduction band. The LSAS behavior (i.e., the interlayer charge transfer) ends when the entire upper Hubbard band rises above the conduction band. Based on our Hall measurement, the estimated

amount of charge transferred in the LSAS regime in our devices is well within the density of the first moiré band at low twist angle.

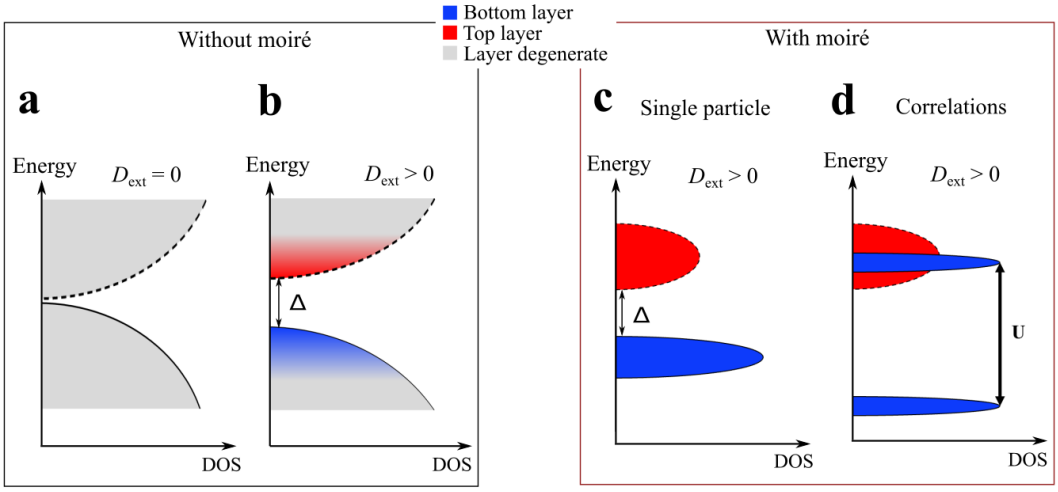

Figure S5: Illustration of the spontaneous charge transfer process due to on-site Coulomb repulsion. For all the schematics, the x axis is the density of states (DOS) and the y axis is energy. The schematics are simplified to help understanding. **a-b,** For normal Bernal-stacked bilayer graphene (no superlattice) without an external displacement field, valence and conduction bands touch at a single point. **b,** The external displacement field opens up a band gap with layer polarization at its band edges. **c-d,** For Device H4, due to the formation of moiré superlattice, the bandwidth is significantly reduced. When applying an external displacement field, the low energy bands can be almost fully layer-polarized, meaning that the electron wavefunction of the valence band is completely localized in the bottom layer while the electron wavefunction of the conduction band is completely localized in the top layer. If we further introduce correlation effects for the valence band (assuming that the valence band is flatter), the on-site Coulomb repulsion will generate a Coulomb gap at half filling. The top Hubbard band can be pushed above the bottom of the (red) conduction band (which is associated with the top layer). Such a change to band sequence could induce a spontaneous charge transfer process, which means electrons transfer from the bottom layer to the top layer in real space.

Comparison between Device H4 and Device H2: We compare important properties between H4 and H2.

Similarities: 1. Both H4 and H2 show strong hysteresis. 2. Both H4 and H2 show the LSAS behavior. 3. Because of the LSAS behavior, an external displacement field can change the mobile charge density in both H4 and H2. 4. The remnant polarization in H4 and H2 are on the same order of magnitude (0.1 μC·cm^{-2}). In fact, we have observed similar behavior in multiple devices (SI.V.4). The polarizations are all on the same order of magnitude.

Distinctions: 1. The sequence between the normal bilayer graphene behavior and LSAS behavior is the opposite. For example, starting from $D_{ext} = 0$, let us consider the situation as we increase D_{ext}. H4 first shows the normal bilayer graphene behavior. When $D_{ext} > D_1$, H4 shows the LSAS behavior. On the other hand, H2 first shows the LSAS behavior. When D_{ext} is larger than a critical value, H2 shows normal bilayer behavior. This difference leads to different P-D_{ext} loops, which will be described below. 2. One may easily notice that the gate showing the LSAS behavior is opposite for H4 and H2. In H4 (H2), the back gate (top gate) shows the LSAS behavior. However, we wish to note that we have also made devices whose behaviors are more similar to H2 in terms of the sequence between the normal bilayer graphene behavior and LSAS behavior but the back gate shows the LSAS behavior. We believe that which gate shows the LSAS behavior probably depends on which graphene layer has a stronger moiré potential leading to a layer-specific moiré flat band. It is unrelated to the sequence between the normal bilayer graphene behavior and LSAS behavior.

We believe that the ferroelectricity and the LSAS behavior in both devices H4 and H2 can be understood by the layer-specific moiré flat bands and inter-layer charge transfer picture. In Device H4, the flat band is absent at $D_{ext} = 0$. Applying finite D_{ext} opens a bandgap and reduces the width of the band. At a critical

D_{ext}, the band (particularly, valence band) is narrow enough to show correlation-driven charge transfer and polarization. As a result, Device H4 shows the normal bilayer graphene behavior first and then the LSAS behavior due to the correlation-driven charge transfer. In Device H2, it is possible that the single-particle band structure is already quite flat and the correlation effect is already significant. Moreover, the top and bottom moiré potentials are more different due to the 0° and 30° alignment. As a result, charge transfer can occur spontaneously even at zero D_{ext}, leading to the LSAS behavior. When a particular fraction of the moiré band is filled (or depleted) by the transferred charge, normal bilayer behavior will appear.

The behaviors of Devices H2 and H4 suggest that both the displacement field and the details of the moiré structures can determine how flat the band is and how strong the correlation effect is. We note that this is quite likely in our system due to the following: (1) In Bernal bilayer graphene, as a function of the displacement field, the shape of its band structure changes dramatically from "parabolic" to "Mexican hat" for the low-energy electrons; (2) The moiré band structure will further depend on the moiré periodicity and the moiré potential strength. We note that recent experiments on twisted double bilayer graphene show correlated insulator behavior only at intermediate displacement field ranges [22–25]. Those observations suggest the tuning of the bandwidth by displacement field is strongly affected by the moiré potential in a non-trivial way. In our system, the coexistence and independent configuration of the top-BN/graphene moiré potential and bottom-BN/graphene moiré potential will further fine-tune both the single-particle band structures and the correlation landscape, giving rise to different behaviors in Devices H4 and H2.

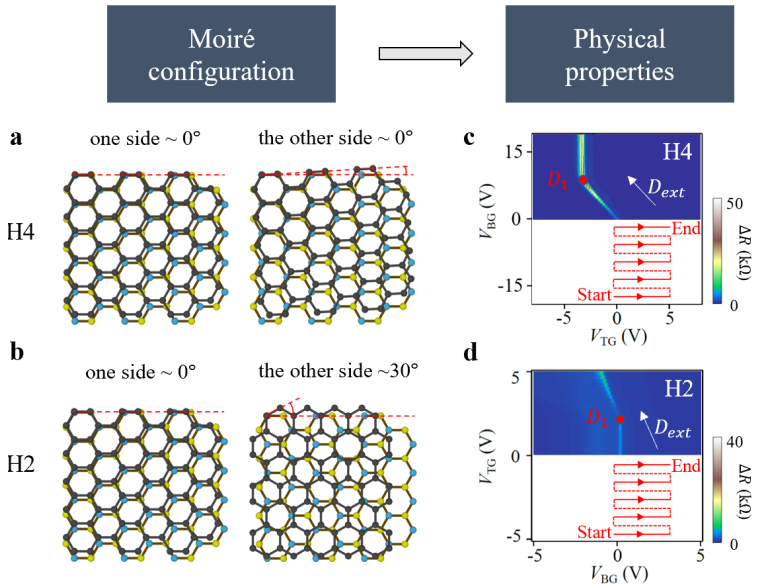

Figure S6: Illustration for interplay among moiré configuration and physical properties. Moiré schematics for **a,** Device H4 and **b,** Device H2. **c,** Dual-gate map for Device H4: V_{TG} is the slow scan axis, V_{BG} is the fast scan axis. **d,** Dual-gate map for Device H2: V_{BG} is the slow scan axis, V_{TG} is the fast scan axis. The white arrows denote the displacement field axis in **c** and **d**.

P-D_{ext} schematics: After explaining the LSAS behavior based on the interlayer charge transfer picture, we schematically map out the electrical polarization (P) as a function of the external displacement field (D_{ext}). Here, the P has two contributions, the polarization generated by the external displacement field and the spontaneous polarization due to interlayer charge transfer.

For device H4, we start by considering the forward scan. The system behaves as the normal bilayer graphene below D_1. Therefore, in this region, the polarization P has one contribution, i.e., the polarization generated by the external displacement field. Upon reaching D_1, the "anomalous screening" occurs. As explained above, the interlayer charge transfer contributes a spontaneous polarization which is in the opposite direction of the externally applied positive displacement field. Therefore, the polarizability, defined as $\frac{\partial P}{\partial D}$, decreases. This manifests as a decrease of the slope in the $P - D_{\text{ext}}$ schematic. When the displacement field scanning direction is reversed, the system recovers the normal bilayer graphene behavior. Upon reaching D_2 in the backward scan, we enter the "anomalous screening" regime, which, again, leads to a decrease of

the polarizability. As such, the polarization P at $D_{\text{ext}} = 0$ for the forward scan is positive, whereas the polarization P at $D_{\text{ext}} = 0$ for the backward scan is negative, as depicted in Fig. S7**a**. This is consistent with observations in Fig. 3**a** in the main text.

We can similarly sketch the $P - D_{\text{ext}}$ dependence for Device H2. However, there are some interesting differences between Devices H2 and H4. As mentioned above, a prominent difference is the sequence of the normal bilayer graphene behavior and "anomalous screening" behavior. In Device H2, the forward scan first shows the "anomalous screening" behavior and then the normal bilayer graphene behavior. Based on this, we can sketch the $P - D_{\text{ext}}$ dependence for Device H2, as shown in Fig. S7**b**. For H2, the polarization P at $D_{\text{ext}} = 0$ for the forward scan is negative, whereas the polarization P at $D_{\text{ext}} = 0$ for the backward scan is positive. This is consistent with observations in Fig. 3**b** in the main text.

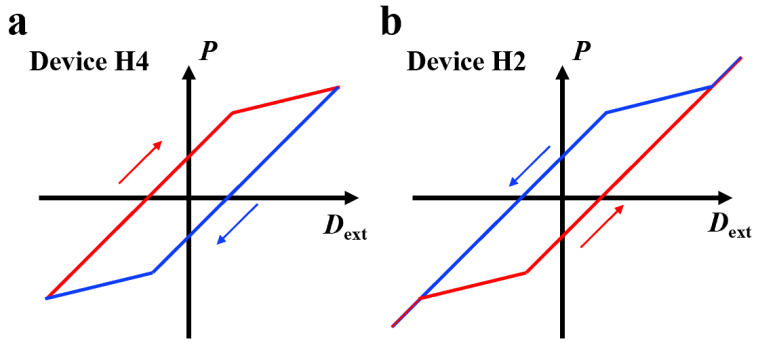

Figure S7: Schematics of electrical polarization (P) as a function of the external displacement field (D) for **a,** Device H4 and **b,** Device H2.

In the main text, we mentioned that the reversed $P - D_{ext}$ loop is energetically possible due to the Δn feature in our system. Here, we will elaborate on this point based on the above proposed picture. When considering the internal energy of the system, we should consider both E,P and μ,n:

$$dU = EdP + \mu dn$$

where μ is chemical potential and n the number of electrons per unit area. One can show that the contribution of EdP over a hysteresis loop is essentially the area of the $P - E$ loop, the sign of which is determined by whether it is clockwise or counter-clockwise (Fig. S8**g**). A clockwise $P - E$ loop implies a reduction of the system's internal energy over a closed cycle.

On the other hand, because the system exchanges particles with the ground, we also need to consider the $-\mu dn$ term. We have now considered the course of μ and n over a cycle with the model provided in the main text and indeed obtained a counter-clockwise $\mu - n$ loop as shown in Fig. S8**h**. Therefore, the sum of EdP and μdn term over the cycle may be positive.

Specifically, we study a hysteresis loop as a function of D-field defined by ①-⑥ as noted in Fig. S8**e,f**. The evolution of n can be directly obtained from our Hall measurement data. The evolution of μ can be inferred based on our microscopic picture. Specifically, since the BLG is grounded, the sum of chemical potential μ and the electrostatic potential ϕ for the electrons at the Fermi level is always zero, namely, $\mu + \phi = 0$. In BLG, the overall electrostatic potential ϕ can be considered as $\phi = (\phi_t + \phi_b)/2$, where ϕ_t and ϕ_b are the electrostatic potential energy (of electrons) of the top and bottom layers. Therefore, we can derive the evolution of chemical potential μ from the evolution of ϕ_t and ϕ_b.

1. Along Path ① of the $P - D_{\text{ext}}$ loop, the system is in the normal bilayer graphene behavior regime, which is mapped to a single point in the $\mu - n$ loop (Fig. S8**h**). n is fixed because no charge is exchanged with the ground. μ is also fixed for the following reasons: The application of D_{ext} changes ϕ_t and ϕ_b in opposite directions (Fig. S8**a**) but $\phi = (\phi_t + \phi_b)/2$ stays constant. For instance, with a positive, increasing D_{ext}, ϕ_t increases while ϕ_b decreases. We can arrive at the same conclusion from the band structure diagram. As shown in Fig. S8**b**, ϕ_b can be defined as the energy difference from the band representing the bottom layer (the blue band) to the ground; ϕ_t can be defined as the energy difference from the band representing the top layer (the red band) to the ground. With increasing D_{ext} field (Fig. S8**b**), the red band moves up whereas the blue band moves down. Thus, ϕ_t increases but ϕ_b decreases; $\phi = (\phi_t + \phi_b)/2$ stays constant; μ stays constant.

2. Point ② of the $P - D_{\text{ext}}$ loop represents the critical displacement field where the switching between the normal bilayer graphene behavior and LSAS occurs. At point ②, μ jumps but n remains constant. Therefore, point ② is mapped to a horizontal line in the $\mu - n$ loop (Fig. S8**h**). This conclusion is derived as follows: within our model, a Hubbard gap opens up at point ② (blue band splits into the upper and lower Hubbard bands shown in Fig. S8**c**). Therefore, ϕ_b jumps up whereas ϕ_t remains constant; $\phi = (\phi_t + \phi_b)/2$ jumps to a positive value; μ jumps to a negative value.

3. Next, along Path ③ of the $P - D_{\text{ext}}$ loop, the LSAS occurs. In this regime, the combination of V_{BG} and V_{TG} cannot keep a constant n; instead, electrons are drained out from the system to the ground along Path ③. Therefore, n decreases continuously and Path ③ is mapped to a line pointing downward in the $\mu - n$ loop.

4. We can further finish the loop by analyzing the rest of the cycle as shown in Fig. S8**h**. It is straightforward because ④, ⑤, and ⑥ are similar to ①, ②, and ③, respectively, except that the red band becomes the valence band whereas the blue band becomes the conduction band.

While we provided a possible scenario above, we do wish to acknowledge that the evolution of μ in the loop is based on our theoretical picture. Our current measurements do not provide a direct measure of chemical potential. Also, even if the $\mu - n$ loop does contribute to a positive area, one would need that the area contributed by $\mu - n$ to compensate for the contribution by EdP. This cannot be rigorously proven unless we measure E,P, and μ,n precisely over the cycle. On the other hand, our data clearly show that our system is an open system and that it exchanges charged particles with the exterior. Therefore, only considering the $P - E$ contribution is incomplete and the $\mu - n$ loop must be considered when analyzing the system.

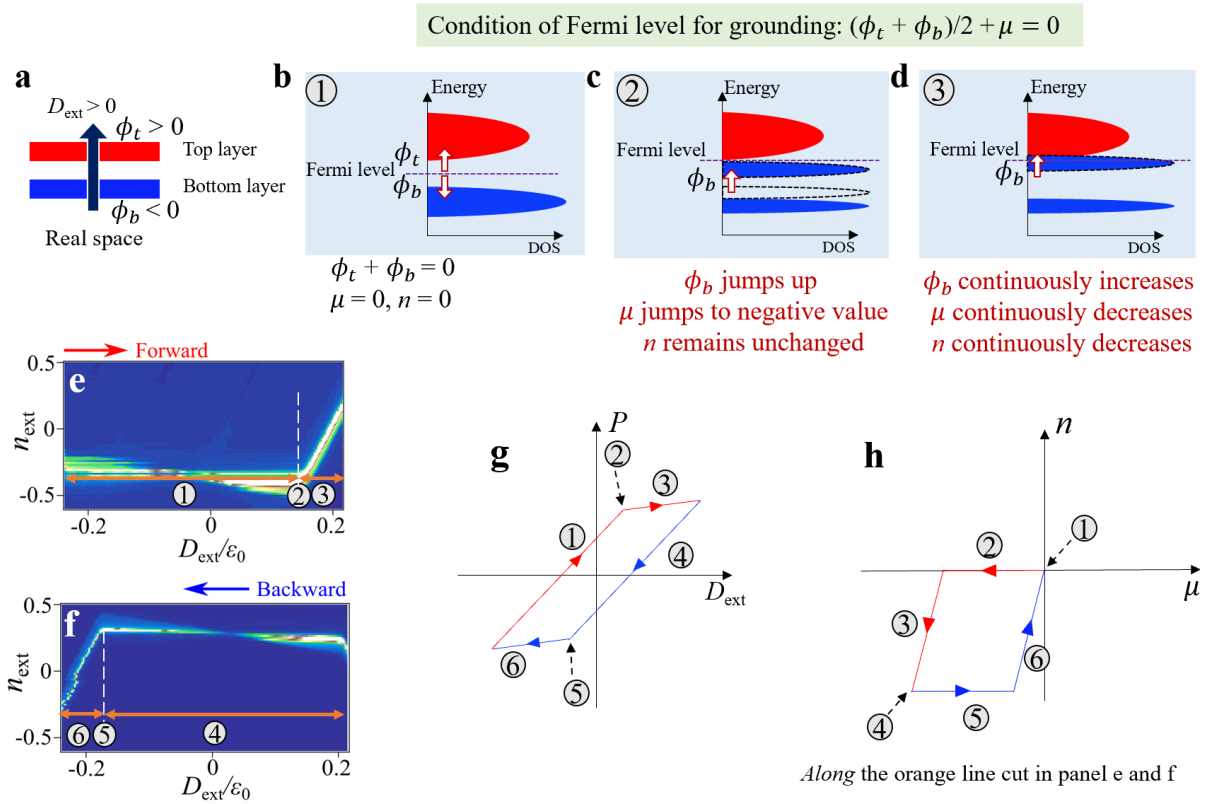

Figure S8: Upper panel: **a,** Schematics of bilayer systems under positive displacement field. **b-d,** Schematics of energy vs. DOS at different stages. Lower panel: Resistance map of $n - D$ scan in **e,** forward and **f,** backward direction. Schematics of **g,** $P - D_{ext}$ loop and **h,** $\mu - n$ loop, when D_{ext} is swept forward and backward, as shown in panels **e,f**.

IV. Band structure calculations

In the previous sections, we have demonstrated the electronically driven nature of the moiré ferroelectricity and suggested a possible microscopic picture that can capture many of the striking features in our data. Here, we consider the non-interacting band structure of Bernal-stacked bilayer graphene with one side aligned hexagonal boron nitride (BN) substrate as shown in Fig. S9. The purpose of this section is only to outline the general trend of the bilayer graphene band structure in a moiré system and its evolution under the interlayer electric field. It is, by no means, a one to one correspondence to the microscopic picture, let alone a complete explanation of moiré ferroelectricity.

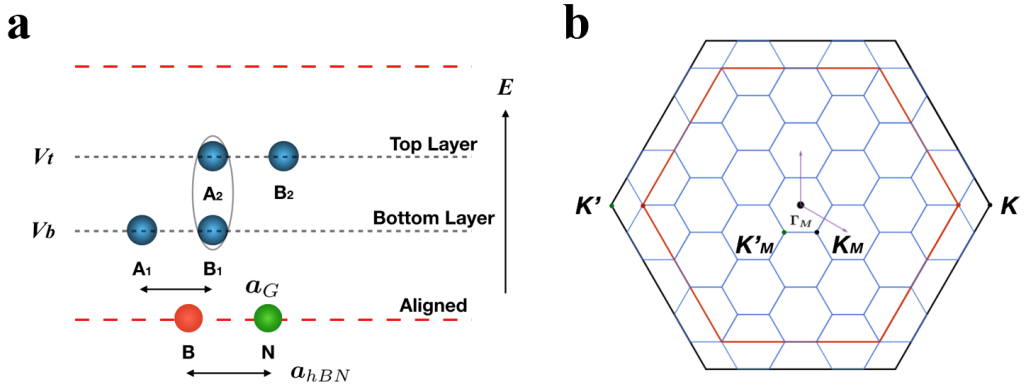

Figure S9: **a,** Schematic plot for the sample. **b,** A demonstration of moiré brillouin zone folding. In our case, the ratio between lattice constants is $a_{\mathrm{BN}}/a_{\mathrm{G}} \cong 1.01786 \cong 57/56$, which has the same folding structure as $a'/a = 6/5$. In this case, the K point of the graphene brillouin zone is folded to the Γ_M point of the moiré brillouin zone.

The moiré Brillouin zone is shown in Fig. S9**b**. The moiré band structure is a function of the interlayer electric field as shown in Fig. S11. We use the continuum model developed in Ref. [29] and the effective model of bilayer graphene given in Ref. [30]. At zero electric field, there is no gap between the moiré conduction band and moiré valence band, as in the case of normal bilayer graphene. No matter how we shift the bottom BN laterally with respect to the bilayer graphene, the calculated band structure remains gapless at zero electric fields, shown in Fig. S10.

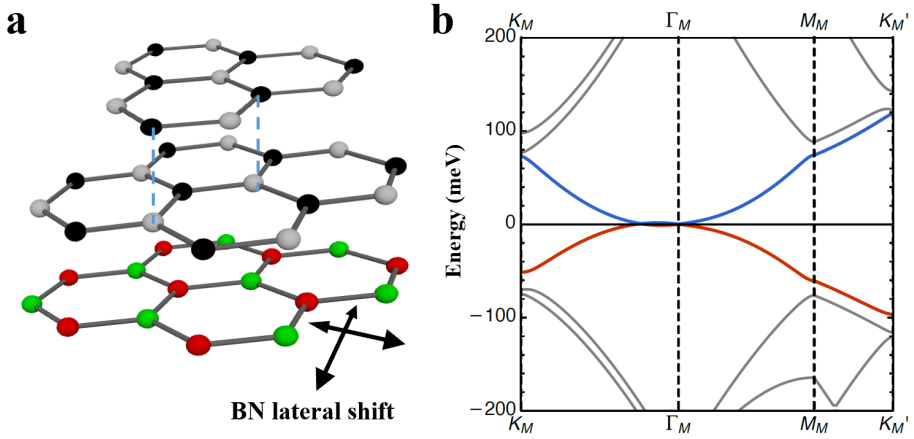

Figure S10: **a,** Schematic diagram for lateral shift of BN with respect to bilayer graphene. **b,** The moiré band structure for $E \cdot d = 0$ meV, where E is the interlayer electric field and d is the interlayer distance.

As we apply an electric field, a gap opens up and the gap size grows with the electric field. The bottommost moiré conduction band and topmost moiré valence band then become increasingly flat. The bandwidth is a monotonically decreasing function of the electric field as shown in Fig. S12**a**.

Besides the gap opening and change in the bandwidth, the polarization of the moiré conduction band and moiré valence band is also changing as a function of the electric field. As mentioned in the previous section, as the electric field increases, the layer polarization starts from the band edge and expands outward. The calculated percentage of the layer polarization of the topmost moiré valence band is shown in Fig. S12**b**. A large layer polarization can be achieved in the low energy moiré bands within a reasonable electric field range.

The case with both top and bottom BN aligned is qualitatively similar to the single side aligned case.

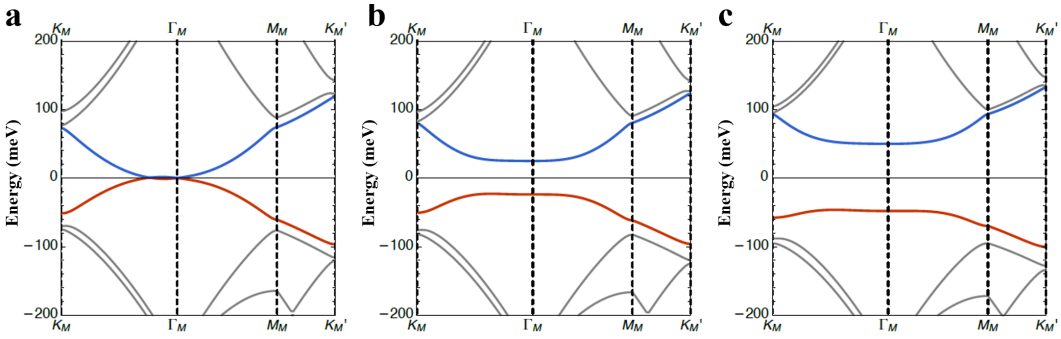

Figure S11: The moiré band structure of graphene/BN moiré at different interlayer electric fields. **a,** $E \cdot d = 0$ meV, **b,** $E \cdot d = 50$ meV, **c,** $E \cdot d = 100$ meV. The bandwidth W monotonically decreases with increasing interlayer electric field, for instance, **a,** $W \cong 97$ meV, **b,** $W \cong 72$ meV, **c,** $W \cong 52$ meV.

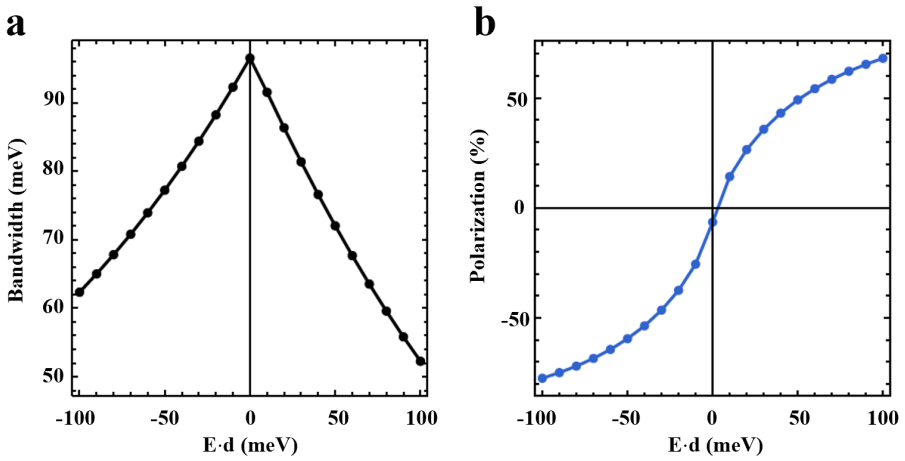

Figure S12: **a,** Bandwidth as a function of interlayer electric field. **b,** Electric polarization as a function of the interlayer electric field.

Due to the unique gate-tunable bandwidth feature in bilayer graphene, U, the onsite repulsion energy, is also dependent on the external electric field. Below, we derive the expression of U and comment on its relation with Δ and W.

What determines U: U, the onsite repulsion energy, is proportional to the overlap integral of Wannier wave-packets on the same site. Therefore, a more essential length scale here is the size of the electron Wannier orbital L rather than the moiré wavelength L_m. In other words, even in a fixed moiré lattice (L_m fixed), U can still vary significantly depending on the size of the Wannier orbital L. In bilayer graphene moiré superlattice, the size of the Wannier orbital L depends on the electric field. As one increases the electric field, electrons can become increasingly localized, meaning a smaller L, leading to a larger U.

To substantiate the picture described above, we derive the expression of U in a moiré lattice under a harmonic approximation. Specifically, we expand the moiré potential at its local minimum in a harmonic approximation. The low energy electrons of bilayer graphene moving in this harmonic potential give rise to the Gaussian wave packet which is an approximation for the Wannier function. This allows us to estimate the size of Wannier orbital and eventually U.

Mathematical derivation:

We can write the moiré potential in the following form:

$$V^{ext}(r) = -2V_0 \sum_{j=1}^{3} \cos(G_j \cdot r + \phi), \tag{S1}$$

in which V_0 is the potential modulation, G_j is the reciprocal vector of the moiré superlattice. This can be expanded at local minimum based on a harmonic approximation and written as

$$v^{\text{ext}}(r) = \left[-6v_0 \cos\phi + \frac{1}{2}\omega^2 (r-R)^2\right], where \quad v_0 = \frac{V_0}{E_0}, \quad \omega^2 = 16\pi^2 v_0 \cos\phi, \tag{S2}$$

If we approximate the low energy electrons with a quadratic dispersion, then the low energy Hamiltonian near a single site reads:

$$H = -\frac{\hbar^2 \nabla^2}{2m^*} + \frac{1}{2} m^* \omega r^2, \tag{S3}$$

where m^* is the effective mass of the low energy electrons. From this, we can obtain the Wannier orbital and calculate the overlap integral:

$$U = \frac{\hbar^2}{m^* a_B} \int dr dr' \frac{|\psi(r,0)|^2 \left|\psi\left(r';\mathbf{0}\right)\right|^2}{|r-r'|} = \frac{\hbar^2}{m^* a_B \xi}\sqrt{\frac{\pi}{2}}, \quad a_B = \frac{4\pi\epsilon_0 \epsilon \hbar^2}{m^* e^2}, \tag{S4}$$

where ξ is the size of the Wannier orbital, which can also be related to the effective mass through:

$$\xi = \sqrt{\frac{\hbar}{m^*\omega}} = \left(16\pi^2 \cos\phi\right)^{-1/4} \sqrt{L_m \lambda} \sim (m^*)^{-1/4}, \quad \lambda = \frac{\hbar}{\sqrt{m^* V_0}}, \tag{S5}$$

Thus, we can ultimately relate the on-site Coulomb repulsion/ interaction strength U with the effective mass:

$$U = \frac{e^2}{4\sqrt{2\pi}\epsilon\xi} \propto (m^*)^{1/4}, \tag{S6}$$

As we mentioned in the manuscript, the moiré bands can become very narrow when we increase the displacement field, which means the effective mass of electrons can be large with increasing displacement field. Therefore, we expect U to be tunable by the displacement field and become large in the large field limit.

We estimate the effective mass using the following crude approximation

$$U = \frac{\hbar^2 G_M^2}{2m^*} \sim W(bandwidth) \rightarrow m^* \sim \frac{\hbar^2 G_M^2}{2W}, \tag{S7}$$

where G_M is the linear size of the moiré Brillouin zone. With this estimated effective mass and the moiré potential strength, we can estimate the strength of on-site Coulomb repulsion.

Calculating U, W, and Δ: Following the derivation above, which shows that $U \propto (m^*)^{1/4}$, we now calculate U, W and Δ(bandgap) as a function of the difference of on-site potential energy between the two layers $(\phi_t - \phi_b)$ based on the simple kp model provided above. We note that, in our simple model, $(\phi_t - \phi_b)$ equals the band gap Δ and scales with D_{ext}. As shown in Fig. S13, we see that both Δ and U increase whereas W decreases with increasing $(\phi_t - \phi_b)$.

Before we further proceed, we wish to caution that this is a model for BLG aligned with BN on one side, whereas the other side of the BLG is bare, without BN. To theoretically simulate the structure used in our experiments is quite challenging and requires advances in theory. The current theoretical calculation may be used as a rough guide that may capture some of the important aspects of the physics, such as the opening up of the band gap and the flattening of the bands with increasing displacement field.

Experimentally, in Device H4, the upper bound of the band gap at the transition to the LSAS behavior is found to be $\sim$ 90 meV based on thermal activation measurement. We now return to the theoretical calculation (Fig. S13). Since, in our model, $(\phi_t - \phi_b)$ equals the band gap Δ, the band gap Δ (blue dashed line) is a straight line with the slope of 1. Within the range of the band gap achieved in experiments ($\sim$ 90 meV), our calculations in Fig. S13 show $\Delta < U$. Therefore, if a Hubbard gap opens (with W reduced to a

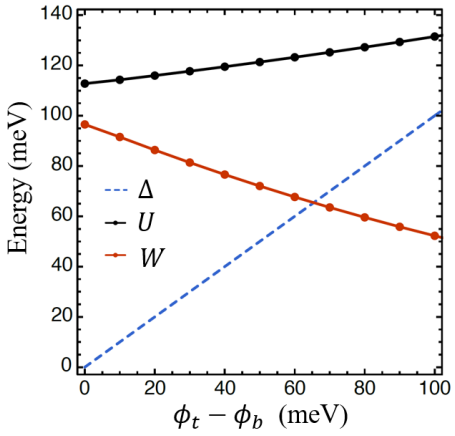

Figure S13: Calculation of Δ, u, and W as a function of the layer potential energy difference ($\phi_t - \phi_b$).

critical value), the system will enter the charge transfer regime, meaning that once a Hubbard gap opens in the valence band, the top of the valence band moves above the bottom of the conduction band.

What determines the conditions under which the Coulomb gap opens: In general, a Mott transition happens when the ratio U/W reaches an O(1) number (W is the bandwidth of the moiré band). The exact critical value of U/W for a Hubbard gap to open up depends on many details of the system, which requires more sophisticated numerical study such as quantum Monte Carlo or DMRG. In our case, the actual band structure details remain unknown. Therefore, a more detailed theoretical calculation of the electric field driven charge transfer transition is perhaps more useful after future experiments have determined the detailed band structure of our devices. Presently, we know from our data that the field-driven transition is first-order because of the strong hysteresis. Thus, we do not expect universal scaling behaviors near the critical point.

Irrespective of these details, we emphasize that our preliminary calculation shows that we are indeed in the $\Delta < U$ regime which corresponds to a charge transfer transition, which is consistent with our experimental findings.

Remnant polarization and band polarization: In the main text, we measured the remnant polarization experimentally. In the above band calculation, we estimate the band polarization. Though these two quantities are different, we can relate them through the proposed interlayer charge transfer picture. The surprising agreement between the two further validates our theoretical picture and experimentally obtained polarization.

First, We want to make a note about how we obtain the ferroelectric polarization from our data. As described in the main text, the gapless point is achieved when the total displacement field in between two graphene sheets is zero, *i.e.*, $D_0 = 0$. From this, we have the internal polarization equals the opposite of the externally induced field, which can be approximated as the averaged electrical displacement field induced by the top and bottom gate, *i.e.*, $D_{\text{ext}} = \frac{1}{2}(\frac{\varepsilon_b \varepsilon_0 V_{\text{BG}}}{d_b} - \frac{\varepsilon_t \varepsilon_0 V_{\text{TG}}}{d_t})$. Therefore, we have $P = -D_{ext}$. Here, we only consider the ferroelectric polarization. In principle, it is more precise to consider both the paraelectric and ferroelectric polarization. In that case, one would have $P = P_{para} + P_{ferro} = -D_{ext}$. The paraelectric polarization was found to be proportional to D_{ext} (*i.e.*, $P_{para} = \alpha D_{ext}$) by previous works and was experimentally measured to be ~ 0.8 [14]. Therefore, this additional consideration will not change the results in terms of the order of magnitude. We wish to note that, our goal was to give an order of magnitude estimate for the ferroelectric polarization. Indeed, we obtained the ferroelectric polarization by two independent methods, (1) this method $P = -D_{ext}$ at the gapless point and (2) the top monolayer graphene sensor as described in methods and Extended data Fig. 6. Both methods gave consistent polarization on the order of $0.1\ \mu C/cm^2$, which further confirms the validity of the obtained polarizations.

Next, we want to clarify on band polarization. In our model, we calculate the paraelectric polarization in the following way: The calculated paraelectric polarization is essentially the percentage of layer polarization of the topmost moiré valence band in an external electric field. Mathematically, it is then defined as the following,

$$P_1 = \sum_{k \in BZ} |\psi_{A_b}(k)|^2 - |\psi_{B_t}(k)|^2, \tag{S8}$$

where $\psi_{A_b}(k)$ and $\psi_{B_t}(k)$ are components on the A_b and B_t sublattices of the Bloch wavefunction from the first moiré band. This calculation only considers the paraelectric polarization in response to the electric field without the consideration of ferroelectric ordering.

In order to make a quantitative comparison between theoretical calculation and experimental data, we make the following further assumptions based on our charge transfer picture in the following steps:

1. In this picture, we can estimate the magnitude of the ferroelectric polarization from the amount of charges transferred from one layer to the other due to the opening of the Coulomb gap. At near 0 degrees alignment between the graphene and BN, the density of the first moiré band is about $2.5 \times 10^{12} cm^{-2}$.

2. The portion of the first moiré band that contributes to the ferroelectric polarization depends on device details and range of the displacement field. As a rough estimation, we can assume that electrons occupying half of the first moiré band take part in the charge transfer, *i.e.*, $1.25 \times 10^{12} cm^{-2}$. We then multiply this density with the calculated band polarization, we can get the ferroelectric polarization.

3. From our model calculation, we take a characteristic band polarization $\sim 70\%$ at $E \cdot d = 100$ meV. Therefore, the ferroelectric polarization is $1.25 \times 10^{12} cm^{-2} \times 70\% = 0.875 \times 10^{12} cm^{-2}$. In the experiment, we measured the remnant polarization to be 0.05 $\mu C \cdot cm^{-2}$ which converts to $0.3 \times 10^{12} cm^{-2}$.

Therefore, our estimation of ferroelectric polarization based on our calculated band polarization and interlayer charge transfer picture is in line with our experimentally measured remnant polarization. We do want to caution that our band polarization calculation is based on a one-side alignment BLG/BN moiré superlattice in a single particle picture with no correlation. Our proposed interlayer charge transfer is the key to relate the band polarization to ferroelectric ordering. A more accurate estimation will necessarily rely on a better understanding of the band structure, either through theoretical investigation or spectroscopic studies. Nevertheless, our current estimation is already at the same order of magnitude with the measured value, rendering our interlayer charge transfer picture a plausible theoretical explanation and our observation of ferroelectricity an experimentally sound case.

V. Additional data and analyses

V.1. Device H1

V.1.1. Resistance switching behavior at zero B field:

Device H1 is a dual-gated BLG with flower shape (Fig. S14). The special device structure allows us to measure different local areas of the device.

Main characteristics of Device H1:

- **Misalignment between top and bottom BN:** The top and bottom BN are from two different flakes. According to the optical SHG measurement, top and bottom BN are rotated ≈ 20 degrees (or 80 degrees due to the 60° periodicity of the SHG signal).
- **Clear superlattice peaks:** We can clearly see superlattice resistance peaks appearing on both sides of the charge neutrality line (cyan dashed lines in Fig. S14**e**). Based on the superlattice density n_s, we calculate a moiré wavelength $\lambda \approx 10$ nm and an angle of roughly 1.1°. Noticeably, Fig. S14**e** shows prominent asymmetry between the electron and hole-side and also between $+D_{\text{ext}}$ and $-D_{\text{ext}}$. This asymmetry is more extreme in Devices H2 and H4.
- **Hysteresis (mainly along D_{ext} direction, no Δn behavior):** In Fig. S15, we show as we gradually increase the range of the displacement field, the hysteresis becomes more and more prominent between the forward and backward field scans. Particularly, in panels **b** and **c**, there is a prominent resistance peak on the $D_{\text{ext}} > 0$ side for the forward but on the $D_{\text{ext}} < 0$ side for the backward scan.
- **Robustness:** (1) The device has been measured after a few thermal-cycles and in different fridge setups, always with the same results. (2) Different contact configurations have been tested, yielding the same qualitative results (Fig. S16).

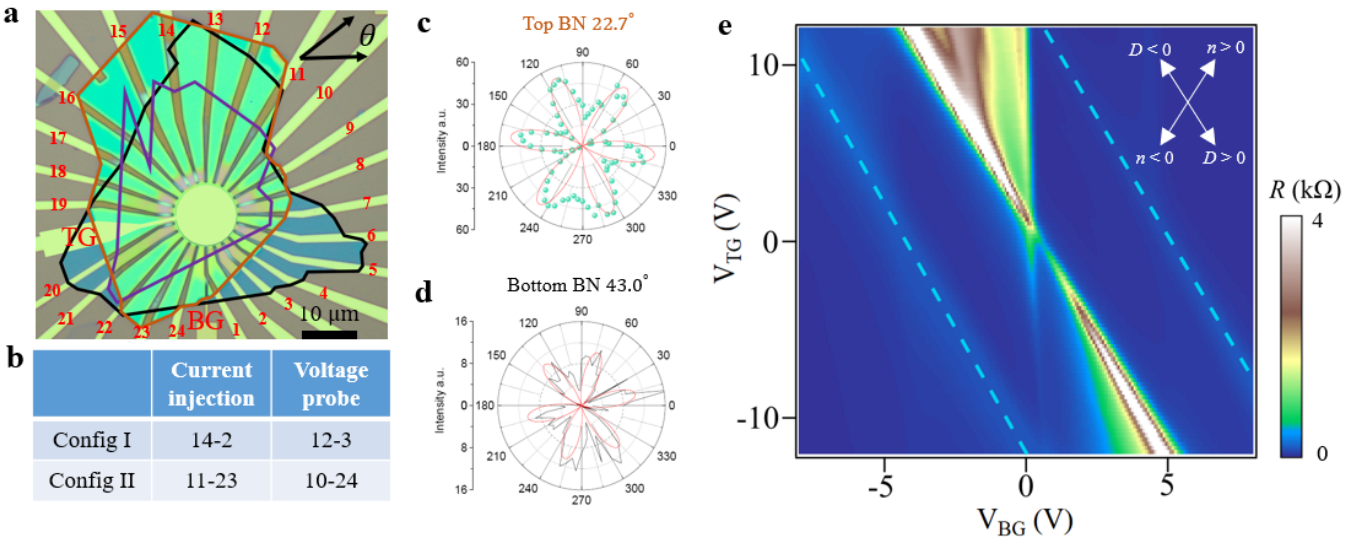

	Current injection	Voltage probe
Config I	14-2	12-3
Config II	11-23	10-24

Figure S14: **a,** The optical image of Device H1. Black, purple and orange outline bottom BN, BLG, and top BN, respectively. **b,** Different measurement configurations defined by current injection and voltage probe contacts. **c-d,** SHG signals for top and bottom BN, respectively. **e,** Dual-gate four-probe resistance map.

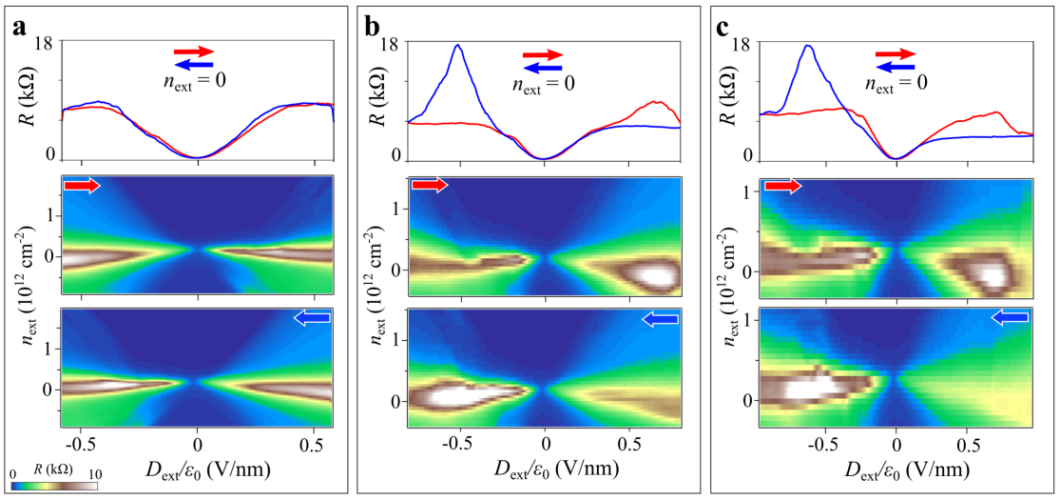

Figure S15: (Configuration I) Resistance hysteresis as the sweeping range of D_{ext} field increases. Line traces are taken at $n_{\text{ext}} = 0$ from the forward and backward $n - D$ maps at each displacement field range. The backward line trace is taken right after the forward line trace for each n.

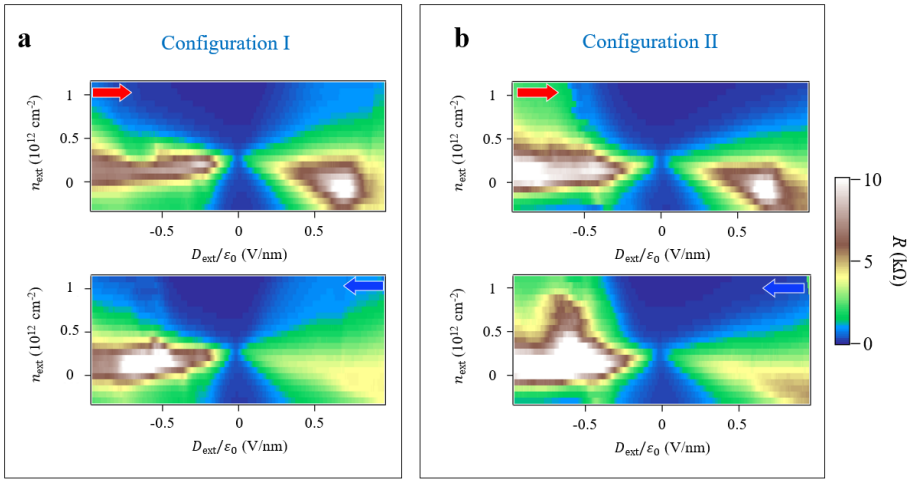

Figure S16: Same measurements as in Fig. S15 panel **c** for two different measurement configurations. Configurations I and II are defined in Fig. S14**b**. Both show the same qualitative results.

V.2. Device H2

V.2.1. Resistance switching behavior at zero B field:

Now, we present additional measurements of Device H2, whose hysteretic $n - D$ maps are shown in the main Fig. 3**b**. During the fabrication of this device, we intentionally aligned the straight edges of both top and bottom BN flakes and graphene (Fig. S17**a**). It turns out that the bottom BN is rotated roughly 30 degree relative to the top BN based on SHG measurements. We made this device in the flower geometry with many electrical connections that allow us to measure different local areas of the sample.

This device was measured over the course of a few months, in different cryostats, and after multiple thermal cycles. The results are extremely robust. We emphasize two important observations:

- **Resistance map is very sensitive to stacking angles:**

  During the fabrication, wrinkles were formed in the stack, as shown in Fig. S17**b**. Such ripples will introduce small angular rotations between adjacent layers. Therefore, areas A, B, and C are expected

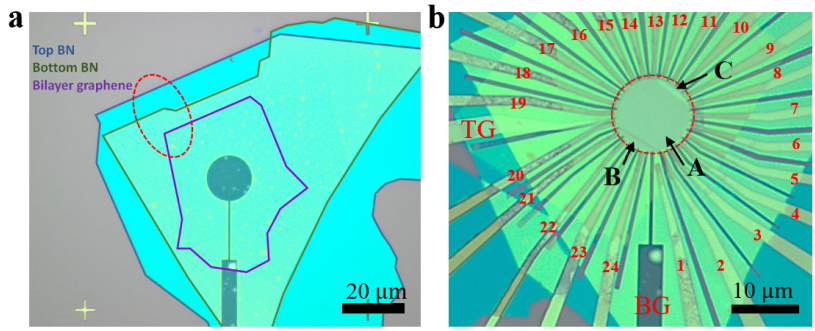

	Current injection	Voltage probe
Config I	14-2	13-3
Config II	21-24	22-23
Config III	8-11	9-10
Config IV	10-22	11-21

Figure S17: Basic information on Device H2. **a,** Optical image of BN-encapsulated BLG stack on the metal bottom gate before contacts were made to the graphene. The red circled area highlights the aligned edges of all three flakes. **b,** Optical image of the final device: 24 contacts, and top and bottom gates. There are two wrinkle lines formed that separate the device into three areas labeled A, B, C. **c,** Four different measurement configurations of current injection and voltage probe contacts. The numbers correspond to the contact labels in **(b)**.

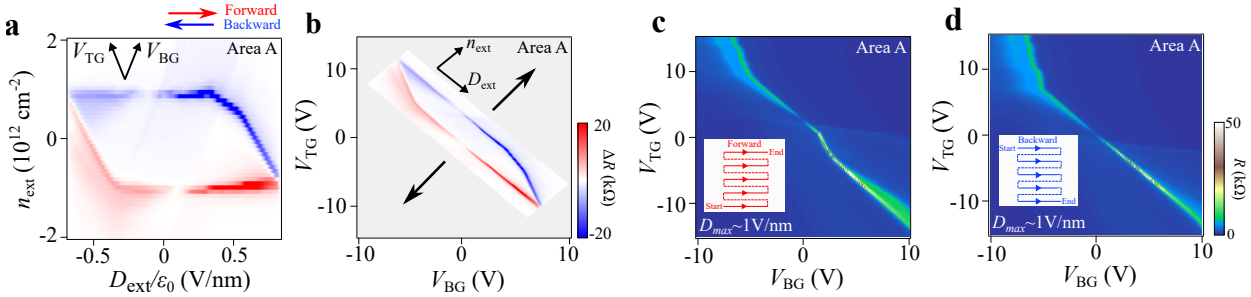

Figure S18: **a,** $n-D$ map for configuration I, which is the same measurement as main Fig. 3**e**. **b,** Converted dual-gated map from panel **(a)**. **c-d,** Dual-gate resistance map. The scanning sequence is shown in the inset.

to have slightly different stacking angles, despite originating from the same graphene and BN flakes. We take advantage of these ripples to explore the dependence of the hysteretic behavior on angle variations by performing four-probe resistance measurements with different electrical configurations, as described in Fig. S17**c**. In Configuration I, the current is injected through contacts 14 and 2, and the voltage is measured across Contacts 13 and 3. The four-probe resistance measured is most sensitive to Area A, the largest area of the device. Similarly, Configuration II primarily measures Area B, Configuration III primarily measures Area C, and Configuration IV measures the combination of all three areas A, B, and C.

In Fig. S19, we show the four-probe resistance maps as a function of both gates for Configurations I-IV. As expected, the resistance features are vastly different. Here are the main observations:

- Panels **(a)** and **(b)** both have a region of "anomalously screened" V_{TG} around the origin. But the extension of such a region is very different between **(a)** and **(b)**.
- In panel **(c)**, at the $D < 0$ side, the resistance peak is sharply broken into pieces along two different but parallel diagonal lines.
- The resistance features in panel **(d)** are the richest. It contains all the features of **a-c**.

There are also other interesting features that are beyond our discussions here. In summary, the distinct resistance features in **(a-c)** correspond to areas A, B, C with slightly different stacking angles due to wrinkles. Panel **(d)** combines the features of **(a-c)** because Configuration I contains all three areas. Therefore, we conclude that the transport response is indeed very sensitive to alignment angles. At the same time, since on the large scale, the stacking orders are similar and close to a special arrangement, all the configurations show strong and robust hysteretic behavior, as shown in the $n-D$ maps (Fig. S20).

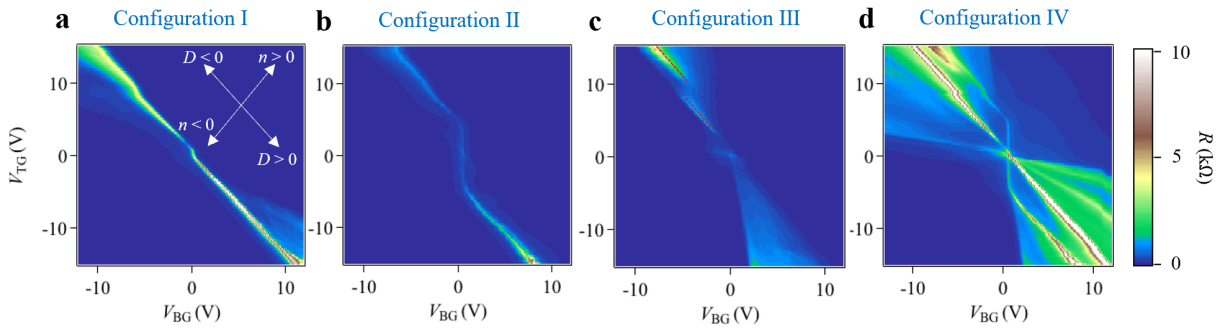

Figure S19: Dual-gate resistance maps for the four measurement configurations labeled in Fig. S17**c**. For all the maps, V_{BG} is the fast scan axis (forward) and V_{TG} is the slow scan axis (forward). The red dashed lines in **(c)** mark the resistance peak positions at $D < 0$.

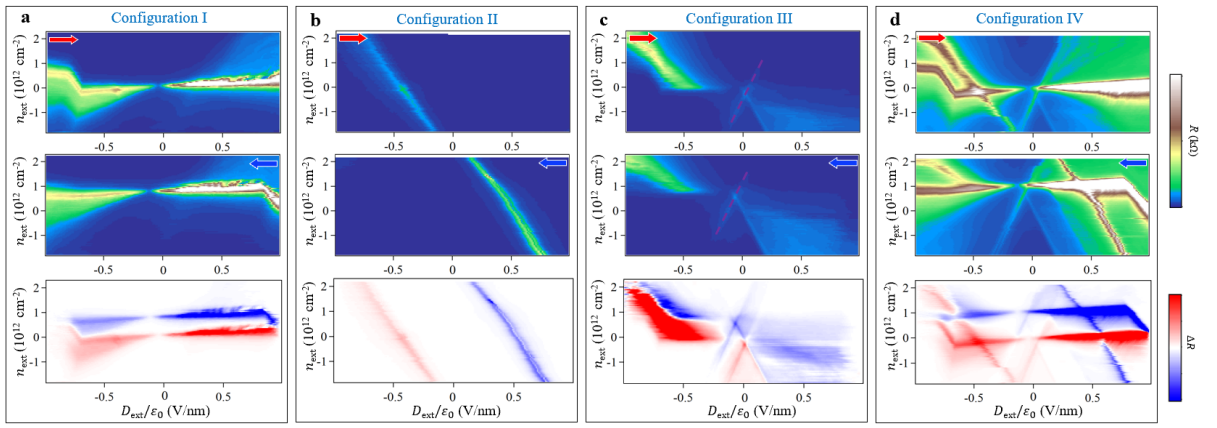

Figure S20: $n - D$ maps (forward, backward scans, and their difference) for the four measurement configurations labeled in Fig. S17**c**. The color scale is 10 kΩ for **(a,d)**, 5 kΩ for **(b)** and 1 kΩ for **(c)**.

- **"Anomalous screening" and its dependence on the sweeping range of D_{ext}:**

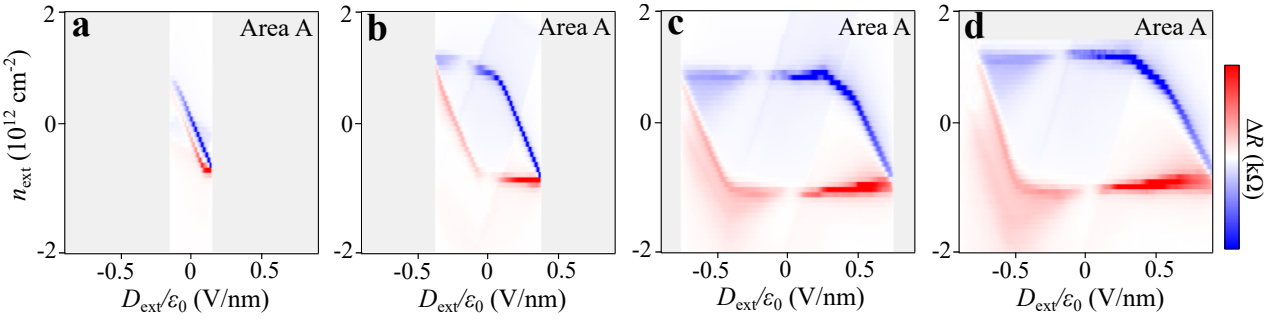

Figure S21: $n - D$ maps (the difference between forward and backward scans) for four different ranges of displacement field in Device H2. The color scale is 10 kΩ for **(a)**, 20 kΩ for **(b-d)**.

Although Devices H2 and H4 show very similar hysteretic "parallelograms" in $n - D$ maps (main Figs. 3**a,b**), there are some key differences and details worth mentioning:

– In Device H4, the "anomalously screened" gate is V_{BG} while in Devices H2, the "anomalously screened" gate is mainly V_{TG}. We add "mainly" here because in Configuration III (Fig. S20**c**), we do see resistance features (with hysteresis) along V_{BG} (purple dashed line), although these

are comparatively weak. This interesting variation, which leads to either V_{BG} or V_{TG} being anomalously screened, points towards the delicate nature of the electronic band structure that is highly sensitive to angle alignments.

– In the main text, we go through the scanning sequence in Device H4 to uncover the onset of the hysteretic behavior in Fig. 2. In comparison, a similar scanning sequence in Extended Data Fig. 3 reveals that in Device H2, the "anomalous screening" behavior appears immediately, followed by normal bilayer graphene behavior. This switching order can also be seen in the $n-D$ map, as shown in Fig. 3**b** and Fig. S21. This also links to a unique feature in Device H2: the "anomalous screening" behavior can occur near the origin ($V_{\mathrm{BG}} = V_{\mathrm{TG}} = 0$), as best shown in Fig. S19**b**.

– In Fig. S21, we demonstrate that we can vary the size of the hysteresis parallelogram in the $n-D$ map by changing the displacement field range. Similar to Device H4, there is a displacement field that separates the normal bilayer graphene and "anomalous screening" behavior in Device H2. While the displacement field range remains below this threshold, there is no switching between the two scanning directions and hence no hysteresis (Fig. S23**a** inset). Once we reach the onset condition, the size of the parallelogram grows as we increase the displacement field range. However, it is worth pointing out that the sides of the parallelogram that corresponds to "anomalous screening" behavior and the value of Δn_{ext} remain fixed while the sides that run horizontally in the $n-D$ map can vary in length. In the next section, we will further show that the parallelogram saturates in size at a large enough displacement field.

V.2.2. Additional capacitance data:

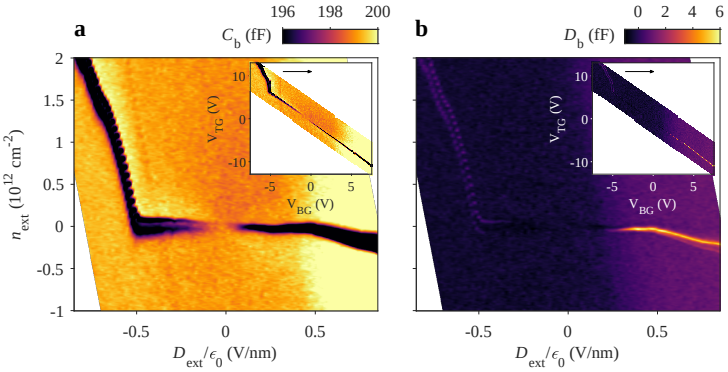

Figure S22: **a,** Bottom-gate capacitance (in-phase) and **b,** dissipation (out-of-phase) signal, sweeping V_{BG} as the fast axis and scanning V_{TG} slowly from top to bottom. Where the dissipation is small (dark regions), the sample is highly conducting and the measurement may be regarded as purely capacitive. In highly incompressible regions, however, the out-of-phase part can increase due to resistive behavior in the lateral charge transport through the bilayer. The data are rotated with respect to the applied gate voltages (shown in insets) and plotted versus the gate-defined displacement field and gate-defined carrier density.

We introduced the capacitance measurement and the basic characteristics of the bottom capacitance measurement in the Methods section and Extended Data Fig. 7. In Fig. S22, we plot both the in-phase (capacitance) and out-of-phase (dissipation) signals accompanying the data shown in Extended Data Fig. 7. The out-of-phase signal is significantly smaller, which demonstrates that our capacitance measurement is valid. To some extent, the capacitance dips correspond to the resistance peaks in transport measurement. In the following, we present systematic capacitance data to show the dependence of the switching behavior on the displacement field range.

In Fig. S23**a**, we show a series of line traces in the back gate capacitance measurement at zero externally gate-defined carrier density, n_{ext}, with an increasing range of displacement field, D_{ext}, in both forward and backward scanning directions. We start from zero displacement field and slowly increase the range of the displacement field. Each time when the forward and backward scans go across the charge neutrality line (the side of the parallelogram as shown in Fig. 3e), there is a dip in the capacitance data. At the beginning, the range of the displacement field is within the "anomalous screening" range, and there is no transition to the

normal bilayer graphene behavior. Thus, there is no hysteresis in the forward and backward scans. As the D_{ext} range increases, the parallelogram grows in size, consistent with Fig. S21. Another feature captured here is that there is an upper bound of the displacement field beyond which the parallelogram stops growing. At large displacement fields, the forward and backward scans overlap with each other as demonstrated in the schematics.

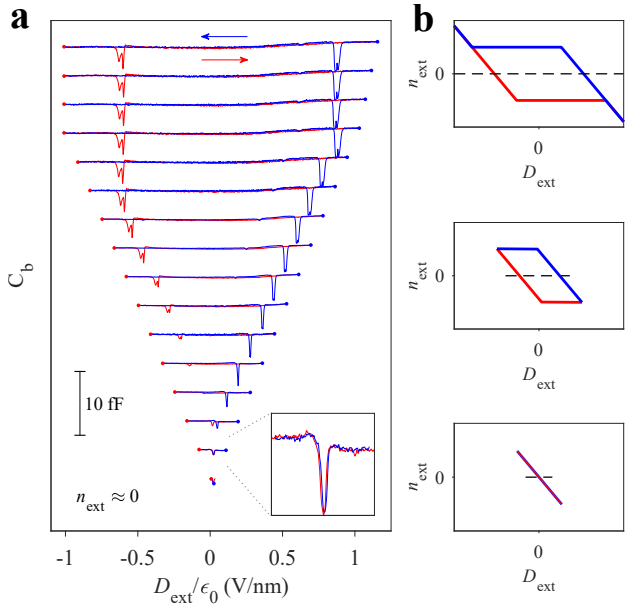

Figure S23: **(a)** Back-gate capacitance measurements with incrementally increasing range of D_{ext} at $n_{\text{ext}} = 0$. Curves are vertically offset for clarity. **(b)** Diagrams that schematically depict the scans from **(a)** as a dashed line in each panel, from top to bottom, representing the approximate sampling region with respect to the hysteretic parallelogram.

V.2.3. Magnetic field dependent measurements:

We also measured how an externally applied magnetic field affects the behavior of this device. Since the magnetic field response is beyond the scope of the current report, we only show some representative measurements and preliminary results. We observed the features of the hysteresis loop evolve gradually under the magnetic field, especially around the zero displacement field regime.

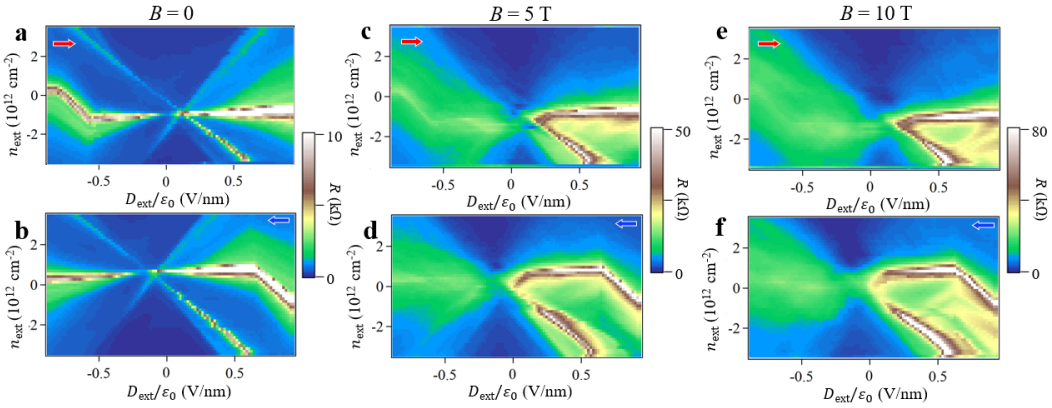

Figure S24: $n-D$ maps (forward and backward scans) at three different B fields. **a-b,** Forward and backward D maps at $B = 0$. **c-d,** Forward and backward D maps at $B = 5$ T. **e-f,** forward and backward D maps at $B = 10$ T.

V.3. Device H4

Device H4 has been discussed in detail in the main text. Here, we show some supplementary data and analyses to further demonstrate the striking behavior of this device.

V.3.1. Resistance switching behavior at zero B field:

- **Dual-gate map with V_{BG} as fast axis:**

In the main text, we focus on the dual-gate maps with V_{TG} as the fast scan axis. Here, we show the results with V_{BG} as the fast scan axis in Fig. S25. Figure. S25**a-b** shows the measurement with V_{BG} within ± 10 V. Within this range, it follows a normal bilayer behavior with no hysteresis, consistent with Fig. 2**a**, in which V_{BG} is scanned as the slow axis. Once the range of V_{BG} is extended to $\approx \pm 25$ V or larger, we again start to see "anomalous screening" behavior and hysteresis. Depending on the scan direction of V_{BG}, the "anomalous screening" regime shows up on the left or right of the gapless point, also consistent with the scenario when V_{BG} is used as the slow scan axis. However, the resistance features between the two scan configurations are not exactly the same. The existence of such differences is consistent with the existence of hysteresis: swapping the fast and slow scan axes changes the history before reaching a particular point in the (V_{BG}, V_{TG}) parameter space. This difference also demonstrates an important fact: Although the hysteresis is most prominent when sweeping V_{BG} back and forth, the history of V_{TG} is equally important because the critical field is determined by V_{BG} and V_{TG} together.

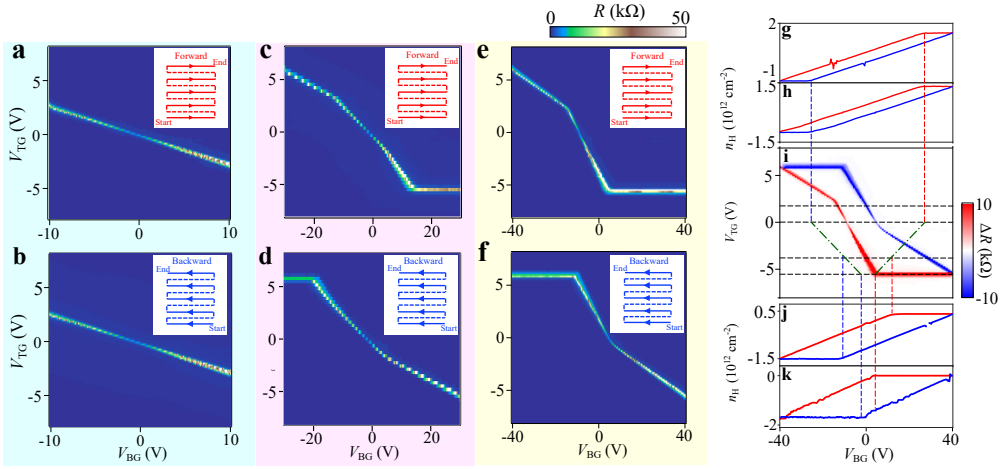

Figure S25: Dual gate resistance map with V_{BG} as the fast scan axis. **a-b,** At each V_{TG}, V_{BG} is scanned forward and backward. The data collected during the forward scan forms **(a)** and that collected during the backward scan forms **(b)**. **c-d,** and **e-f,** are the same kind of measurements but for larger scan ranges of V_{BG}. **i,** The difference between **(e)** and **(f)**. **g-h, j-k,** The Hall density along the dashed lines (from top to bottom) in **i**.

In the main text and sections above, we point out the fact that the gapless point, in the region where the resistance map resembles the normal bilayer graphene behavior, can be moved around in terms of its exact applied top and back gate voltage. By applying an appropriate sequence of gate voltages, its value can be programmed to be far away from the origin. This movement of the gapless point is reversible and its position at the origin can be recovered as follows: In a dual-gate resistance map with the V_{TG} as the fast scanning axis, the "anomalous screening" behavior appears when a relative critical displacement field is reached, corresponding to a well-defined change in the back gate voltage. Depending on how far we travel beyond the critical point, we can change the vertical extent of the parallelogram. If we start from a large negative back gate voltage and scan in the forward direction, when we reverse the scanning direction at a positive back gate voltage with a small magnitude compared to the starting point, we recover the normal bilayer graphene behavior and thus shrink the size of the parallelogram. By repeating this process, we effectively move the gapless point closer and closer to

the origin. Once the range of the back gate voltage is small enough that D_1 and D_2 are not reached anymore, no switching behavior is observed and the gapless point returns to the origin.

- **"Anomalous screening" and its dependence on the sweeping range of D_{ext}:**

  Here, we highlight additional interesting details in terms of the "anomalous screening" behavior and its displacement field dependence:

  – In Fig. 2**j-l**, we show the Hall measurement along the displacement field direction at various nominal carrier densities n_{ext}. One of the main features is that the external field D_1 and D_2 mark the onset of the "anomalous screening" behavior regardless of n_{ext}. This suggests that there is a minimum field that we need to reach before the hysteretic behavior starts to occur at any carrier density. Indeed, as shown in Fig. S21**a**, for a small displacement field range, the $n-D$ map exhibits normal bilayer graphene behavior with no hysteresis.

  – As with Device H2, the enclosed area of the parallelogram in the $n-D$ map can vary with the displacement field range. However, in Device H4, the sides that run parallel to the displacement field remain the same while the sides that correspond to the "anomalous screening" behavior can vary in length. Interestingly, the gapless point can move around in both the dual-gate map and the $n-D$ map but always remains at the same position within the normal bilayer graphene behavior line. Hence, the difference in terms of displacement field value between the gapless point and $D_1(D_2)$ also remains unchanged.

  – As the "anomalous screening" side of the hysteresis parallelogram becomes longer, it enlarges the parallelogram so that the Δn_{ext} between the Dirac peaks of forward and backward scans also increases. Since the relative distance between the gapless point and D_1 and D_2 are fixed, ΔP increases proportionally to Δn_{ext}. In the range of displacement fields we tested, we have not reached a saturation value where the size of the parallelogram stops growing.

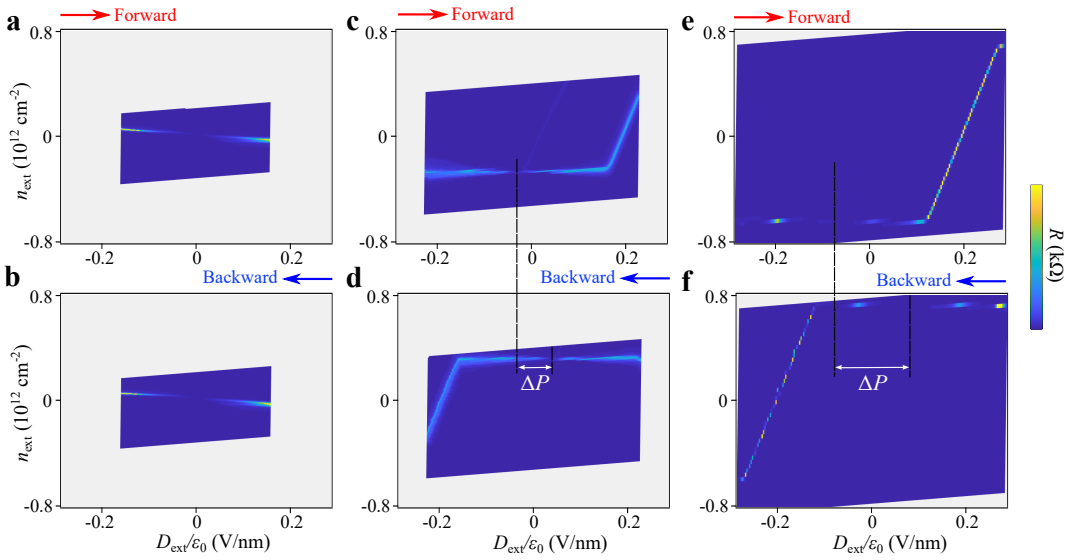

Figure S26: $n-D$ maps (the difference between forward and backward scans) for three different ranges of displacement field in Device H4. The color scale is 50 kΩ for **(a,c)** and 10 kΩ for **(b)**. Four-probe resistance measurement in **(b)** was conducted with a different contact configuration of Device H4, hence the variation of the resistance magnitude.

Following the above descriptions, we expect the remnant polarization to scale with the range of D_{ext}. Below, we extract their relation directly based on our data plotted in Fig.3**a** and Fig. S26. Fig. S26**a,b** show a normal bilayer graphene behavior with no hysteresis at a small scan range of D_{ext}/ϵ_0. The minimum range of D_{ext}/ϵ_0, below which there is no LSAS and hence zero remnant polarization, is determined to be 0.388V/nm from Figs.2**j-l**. In addition, we can read out the remnant polarization as described in the main text with three different scan ranges from Fig.3a and Fig. S26, giving us three additional data points. By plotting out ΔP vs. the scan range of D_{ext}/ϵ_0, we see a clear linear dependence with a slope of 0.7892 and R squared of 0.9985. This is consistent with our speculation that the remnant polarization is linearly proportional to the range of displacement field above the critical field.

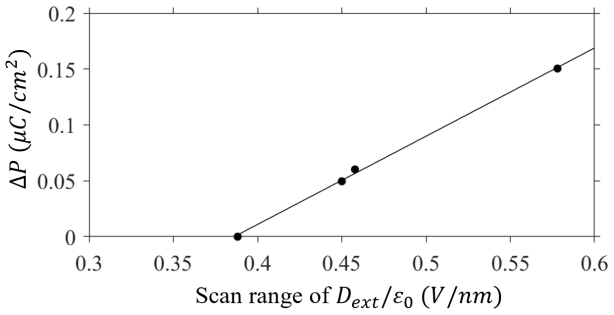

Figure S27: ΔP v.s. Scan range of D_{ext}/ϵ_0

- **Non-monotonic dependence of Dirac peak on D_{ext}:**

In normal bilayer graphene, the single-particle band gap has a linear dependence on the external electric field. However, it is in general hard to infer such linear dependence from the device resistance. Nevertheless, one should expect the resistance along the Dirac peak to show a monotonic trend in the electric field direction. If a non-monotonic trend is observed, it can be a strong indication of the non-linear dependence of the band gap.

In Fig. S28, we plot out the conductance along the charge neutrality for Device N0, H2, and H4. For Device N0, the conductance starts from the gapless point near zero fields and decreases monotonically with the displacement field, consistent with the normal gap-opening behavior. For both Device H2 and H4, besides the apparent hysteresis between the forward and backward scans, the conductance in each curve shows a nontrivial dependence on the displacement field. Significantly away from the gapless point, the conductance stops decrease and even slightly increases. Such a non-monotonic trend of the conductance with the displacement field indeed suggests that the interlayer electric field and/or the band gap depends on the externally applied field in a non-trivial way in our devices.

- **Non-hysteretic gate:**

In the main text, we point out that the special gate for Device H2 and H4 are top and bottom gate, respectively and there is no hysteresis if we scan along the other gate direction. Here, we show our experimental observations.

In order to illustrate clearly the gate dependent hysteresis behavior, we plot out two sets of measurements for both Device H4 and H2 in Fig. S29. The four panels for each of the devices show all combinations of the gate sweeping direction. Apart from some minor shifts from instrumental backlash, there is no obvious hysteresis in the top gate and bottom gate direction in Device H4 and H2 respectively. This is consistent with the data we present in the manuscript that Device H4 shows a hysteretic dependence on V_{BG}, and Device H2 shows a hysteretic dependence on V_{TG}.

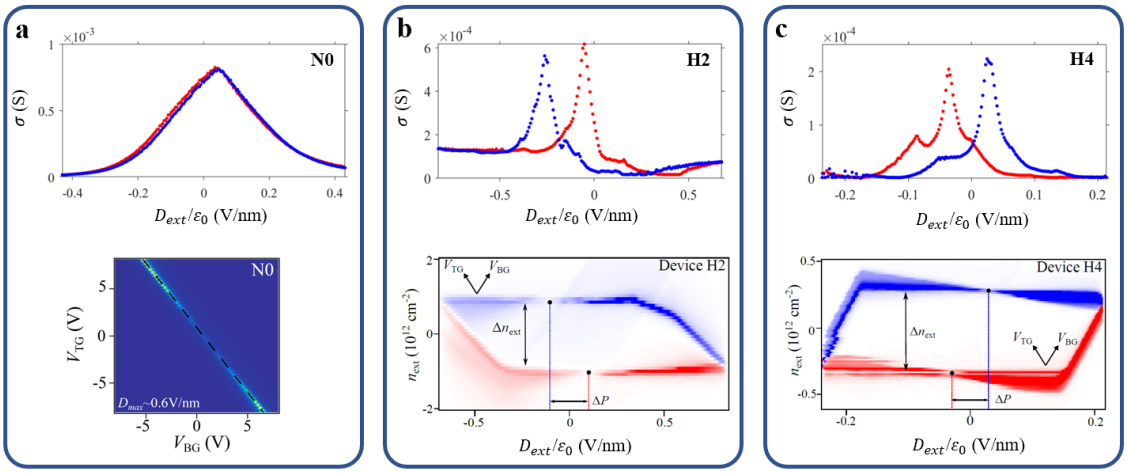

Figure S28: Conductance along Dirac peak as a function of displacement field for **a,** Device N0, **b,** Device H2, and **c,** Device H4.

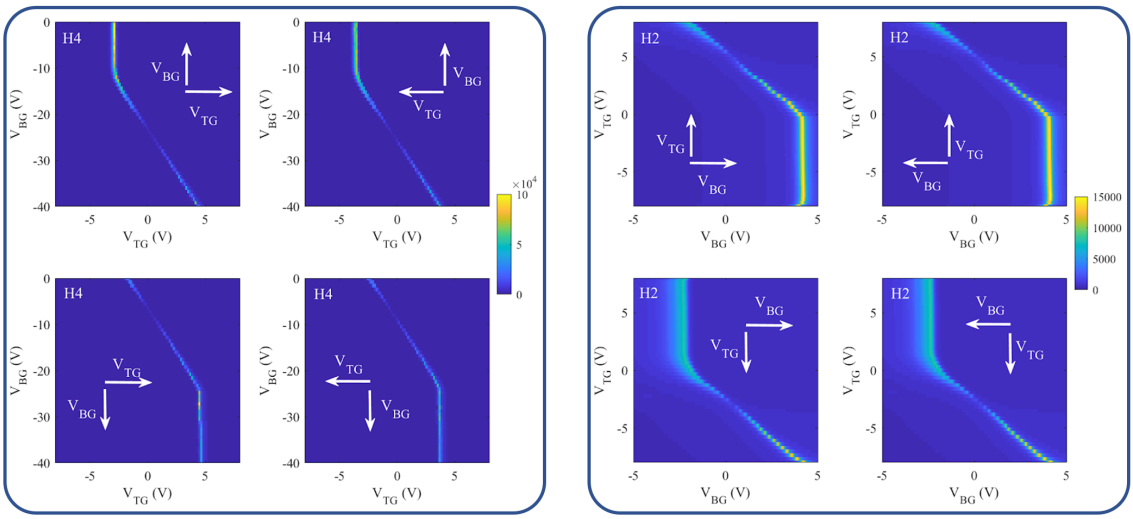

Figure S29: Dual-gate maps for Device H2 and H4 in all scanning configurations.

V.3.2. Transport simulations for Device H4 based on a phenomenological model:

In this subsection, we simulate Device H4's main transport behavior based on a phenomenological capacitance model. This simulation does not involve the microscopic theoretical mechanism for the moiré ferroelectricity. Rather, all the microscopic physics (moiré band structure, correlations, ferroelectric phase transition, etc.) are phenomenologically represented in this simulation by the way in which the top and bottom gates inject charges into the system. We found that, by assuming a definitive but unconventional relationship between the gate voltages and gate-injected charges, we can successfully capture the main data observations such as the strong hysteresis and the "anomalous screening" phenomenon. The purpose is two-fold: First, it provides a simulation of the transport data; Second, it may provide hints and inspiration for a microscopic theoretical understanding of the data, as the way in which the gates inject charges into the system depends on the quantum capacitance and thus the microscopic physics of the electronic state.

In a dual-gated Bernal-stacked BLG, the total carrier density is generally given by $n = n_\mathrm{t} + n_\mathrm{b}$, with n_t and n_b contributed from the top and bottom gates, respectively. With the commonly adopted parallel-plate capacitor model, n_t can be described by $n_\mathrm{t} = (C_\mathrm{t}/e)V_\mathrm{TG}$, where C_t is the top gate capacitance per unit area.

On the other hand, the bottom-gate-contributed carrier density n_b in our experiment exhibits an unusual behavior which cannot be described by the parallel-plate capacitor model (See Fig. S25 for Hall density measured as a function of V_BG). By observation, we found that the following phenomenological model leads to transport simulations that agree well with the experiment:

$$n_\mathrm{b} = \begin{cases} \dfrac{C_\mathrm{b}}{e}[V_\mathrm{BG} - (V_0 + \Delta_V)] \ , & V_\mathrm{BG} < V_0 + 2\Delta_V \\ \dfrac{C_\mathrm{b}}{e}\Delta_V \ , & V_\mathrm{BG} \geq V_0 + 2\Delta_V \end{cases} \qquad \text{(forward sweep)}$$

$$n_\mathrm{b} = \begin{cases} \dfrac{C_\mathrm{b}}{e}[V_\mathrm{BG} - (V_0 - \Delta_V)] \ , & V_\mathrm{BG} > V_0 - 2\Delta_V \\ -\dfrac{C_\mathrm{b}}{e}\Delta_V \ , & V_\mathrm{BG} \leq V_0 - 2\Delta_V \end{cases} \qquad \text{(backward sweep)}$$

Here, parameters $C_\mathrm{b} \approx C_\mathrm{t} \cdot 4/11$ and $\Delta_V = 12$ V are obtained by observations, and V_0 is the initial back gate voltage value for each V_BG sweep. The above phenomenological model is depicted in Fig. S30**a** and **b** for the forward and backward sweep, respectively.

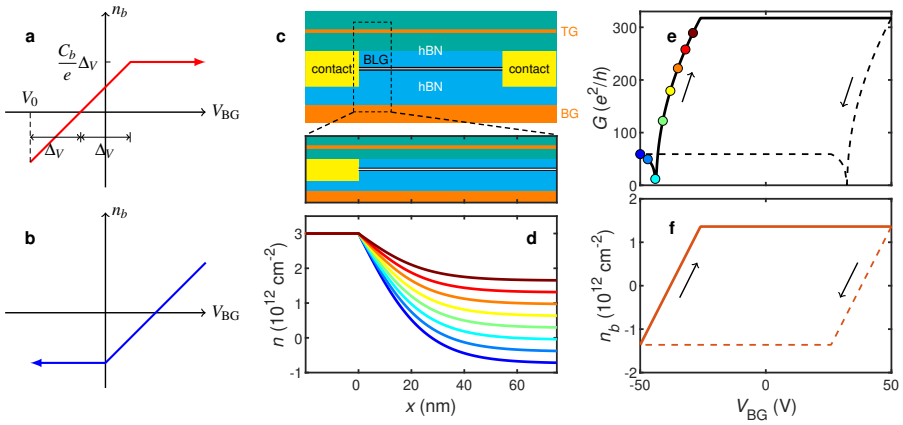

Figure S30: Phenomenological model for the bottom-gate-contributed carrier density under **(a)** forward V_BG sweep and **(b)** backward V_BG sweep. **c,** Schematic of the modeled dual-gated BLG device. **d,** Exemplary carrier density profiles $n(x)$ at $V_\mathrm{TG} = 2$ V and various V_BG, corresponding to the colored circles on the black solid line in **(e)**, which shows the simulated two-point conductance. The dashed line in **e** considers the reversed V_BG sweep. **e,** The phenomenological model function n_b described in **(a)** and **(b)** along the gate voltage sweeps considered in **e**.

Our transport simulations are based on the nearest-neighbor tight-binding model for BLG, using the same

method described in [31]: The model Hamiltonian is composed of the clean part, H_0, along with the onsite energy term,

$$H = H_0 + \sum_{s=\pm 1} \sum_j \left[V(x_j) + s\frac{U(x_j)}{2} \right] c_j^\dagger c_j \ , \tag{S9}$$

where $s = -1$ and $s = +1$ account for the bottom and top layer of the BLG, respectively, and c_j ($c_j^\dagger$) annihilates (creates) an electron on the j-th site located at (x_j, y_j). Furthermore, the band offset profile in Eq. (S9) is given by

$$V(x) = -\mathrm{sgn}[n(x)] \sqrt{\frac{\gamma_1^2}{2} + \frac{U^2(x)}{4} + (\hbar v_\mathrm{F})^2 \pi |n| - \sqrt{\frac{\gamma_1^4}{4} + (\hbar v_\mathrm{F})^2 \pi |n| [\gamma_1^2 + U^2(x)]}} \ , \tag{S10}$$

where $\gamma_1 = -0.39$ eV is the nearest-neighbor interlayer hopping strength, $v_\mathrm{F} \approx 10^6$ m/s is the Fermi velocity of electrons in graphene, and the asymmetry parameter U ($\approx$ gap size) follows Ref. [32] and is a function of top density n_t and bottom density n_b. With the method of periodic boundary hopping [33, 34] implemented, we first compute the normalized conductance g by integrating the two-terminal transmission over the transverse momentum. Assuming the width of the sample to be W, the two-terminal conductance is then obtained by

$$G = \frac{e^2}{h} \frac{W}{3\pi a} g \ , \tag{S11}$$

where a is the lattice spacing. In the following simulations, we consider $W = 1$ μm in Eq. (S11).

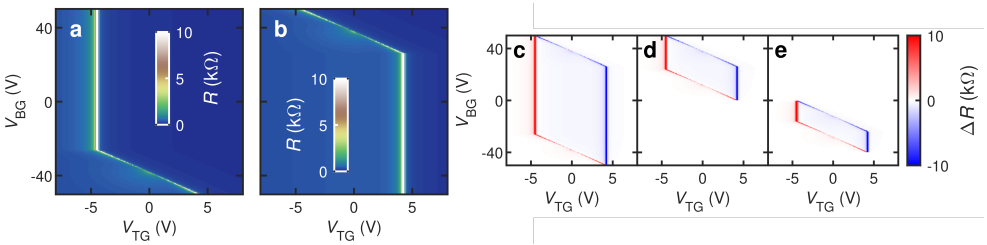

Figure S31: *Simulated* two-point resistance maps with V_TG as the fast axis, and V_BG as the slow axis, for various sweeping ranges of V_BG. **a-b** show forward and backward sweeps for V_BG in the range (-50, 50) V. **c-e** show the resistance difference between forward and backward sweeps for different V_BG ranges.

Our dual-gated BLG device is schematically sketched in Fig. S30**c**. Although the transport behavior of our device is dominated by BLG, we found that the contact doping effect is unavoidable. To demonstrate this, we focus on the junction between the left contact. We model the contact as BLG also, but with pinned top and bottom densities $n_\mathrm{t} = n_0/2 = n_\mathrm{b}$. In the simulations we show here, we take $n_0 = 3 \times 10^{12}$ cm^{-2}, which does not drastically influence the results. Away from the contact, the top and bottom carrier densities are dominated by the gates. The position-dependent profile connecting the pinned and the gate-controlled densities is described by a simple hyperbolic tangent function. A few examples of $n(x) = n_\mathrm{t}(x) + n_\mathrm{b}(x)$ are given in Fig. S30**d**, for $V_\mathrm{TG} = 2$ V and various V_BG along a forward sweep of the back gate. The simulated conductance for this V_BG sweep is shown by the black solid line in Fig. S30**e**, where the circles correspond to the $n(x)$ profiles shown in panel **d**. In this particular sweep, the model function for n_b (away from the contact), as described by Fig. S30**a**, is shown by the solid red line in Fig. S30**f**. The dashed lines in panels **e** and **f** of Fig. S30 consider the backward sweep at the same V_TG.

The forward and backward sweeps of the conductance shown in Fig. S30**e** are line cuts of simulated conductance maps $G(V_\mathrm{TG}, V_\mathrm{BG})$, whose inverse, *i.e.*, the two-point resistance, are shown in Fig. S31**a-b**. In the following, we consider various gate sweeps with V_TG as the fast axis and V_BG as the slow axis. We plot the two-point resistance with forward V_BG sweep in Fig. S31**a** and backward sweep in Fig. S31**b**. The resistance difference between forward and backward sweeps for different V_BG ranges is shown in Fig. S31**c-e** for different ranges of V_BG. Our phenomenological model is able to accurately reproduce the main features of the experimental data and could therefore indicate unusual back gate capacitance behavior in our system.

V.4. Additional Devices

Here we show some additional data on other devices that also show LSAS behavior. We plot them together with Device H2 to demonstrate the similarity in terms of device behaviors.

In Fig. S32, we show a comparison between Device H2 and H5. The top gate is the fast scan axis and the red and blue colors represent the forward and backward scan direction, respectively. The two devices both have the top gate as the special gate, meaning that the LSAS behavior appears in the top gate direction. In addition, both devices show the LSAS behavior first, followed by normal bilayer graphene behavior.

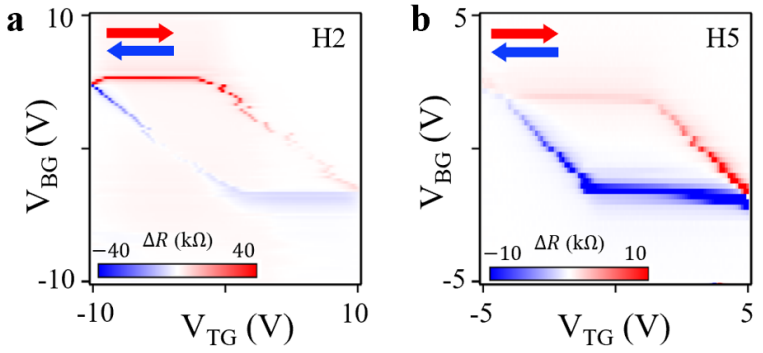

Figure S32: Dual-gate map for Device H2 and H5 with V_{TG} as the fast scan axis.

In Fig. S33, we show a comparison between Device H2 and H6. Device H6 shows a new type of behavior that has the same sequence of LSAS and normal bilayer behavior as Device H2, but the bottom gate is the special gate. This is consistent with our argument that the specific gate shows the LSAS behavior probably depends on the specific graphene layer has a stronger moiré potential leading to a layer-specific moiré flat band. It is unrelated to the sequence between the normal bilayer graphene behavior and LSAS behavior.

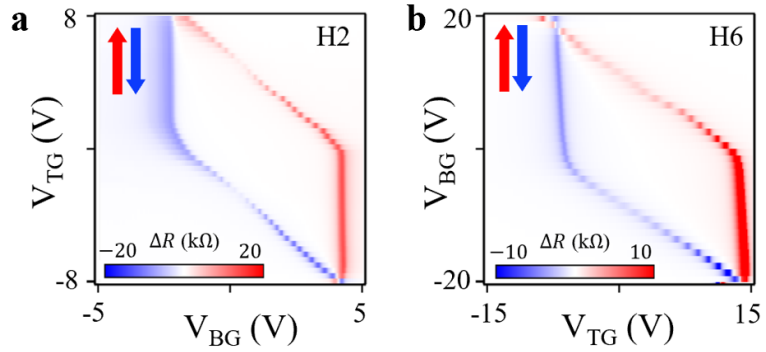

Figure S33: Dual-gate map for Device H2 and H6 with V_{BG} and V_{TG} as the fast scan axis, respectively.

References

[1] McGilly, L. J. *et al.* Seeing moiré superlattices. *arXiv:* **1912.06629** (2019).

[2] Hunt, B. *et al.* Massive Dirac fermions and Hofstadter butterfly in a van der Waals heterostructure. *Science* **340**, 1427–1430 (2013).

[3] Sharpe, A. L. *et al.* Emergent ferromagnetism near three-quarters filling in twisted bilayer graphene. *Science* **365**, 605–608 (2019).

[4] Wang, H., Wu, Y., Cong, C., Shang, J. & Yu, T. Hysteresis of electronic transport in graphene transistors. *ACS nano* **4**, 7221–7228 (2010).

[5] Fei, Z. *et al.* Ferroelectric switching of a two-dimensional metal. *Nature* **560**, 336–339 (2018).

[6] Ribeiro-Palau, R. *et al.* Twistable electronics with dynamically rotatable heterostructures. *Science* **361**, 690–693 (2018).

[7] Song, J. C., Shytov, A. V. & Levitov, L. S. Electron interactions and gap opening in graphene superlattices. *Phys. Rev. Lett.* **111**, 266801 (2013).

[8] Jung, J., DaSilva, A. M., MacDonald, A. H. & Adam, S. Origin of band gaps in graphene on hexagonal boron nitride. *Nature communications* **6**, 1–11 (2015).

[9] Zhang, F., Min, H., Polini, M. & MacDonald, A. H. Spontaneous inversion symmetry breaking in graphene bilayers. *Phys. Rev. B* **81**, 041402(R) (2010).

[10] Nandkishore, R. & Levitov, L. Dynamical screening and excitonic instability in bilayer graphene. *Phys. Rev. Lett.* **104**, 156803 (2010).

[11] Vafek, O. & Yang, K. Many-body instability of Coulomb interacting bilayer graphene: Renormalization group approach. *Phys. Rev. B* **81**, 041401 (2010).

[12] Lemonik, Y., Aleiner, I., Toke, C. & Fal'ko, V. Spontaneous symmetry breaking and Lifshitz transition in bilayer graphene. *Phys. Rev. B* **82**, 201408 (2010).

[13] Maher, P. *et al.* Evidence for a spin phase transition at charge neutrality in bilayer graphene. *Nature Phys.* **9**, 154–158 (2013).

[14] Hunt, B. *et al.* Direct measurement of discrete valley and orbital quantum numbers in bilayer graphene. *Nature Commun.* **8**, 948 (2017).

[15] Weitz, R. T., Allen, M., Feldman, B., Martin, J. & Yacoby, A. Broken-symmetry states in doubly gated suspended bilayer graphene. *Science* **330**, 812–816 (2010).

[16] Bao, W. *et al.* Evidence for a spontaneous gapped state in ultraclean bilayer graphene. *PNAS* **109**, 10802–10805 (2012).

[17] Freitag, F., Trbovic, J., Weiss, M. & Schönenberger, C. Spontaneously gapped ground state in suspended bilayer graphene. *Phys. Rev. Lett.* **108**, 076602 (2012).

[18] Nam, Y., Ki, D.-K., Soler-Delgado, D. & Morpurgo, A. F. A family of finite-temperature electronic phase transitions in graphene multilayers. *Science* **362**, 324–328 (2018).

[19] Chen, G. *et al.* Signatures of Gate-Tunable Superconductivity in Trilayer Graphene/Boron Nitride Moiré Superlattice. *Nature* **572**, 215–219 (2019).

[20] Chen, G. *et al.* Evidence of a gate-tunable Mott insulator in a trilayer graphene moiré superlattice. *Nature Phys.* **15**, 237–241 (2019).

[21] Chen, G. *et al.* Tunable correlated chern insulator and ferromagnetism in trilayer graphene/boron nitride moiré superlattice. *Nature* **579**, 56–61 (2020).

[22] Burg, G. W. *et al.* Correlated insulating states in twisted double bilayer graphene. *Phys. Rev. Lett.* **123**, 197702 (2019).

[23] Liu, X. *et al.* Spin-polarized correlated insulator and superconductor in twisted double bilayer graphene. *Nature* **583**, 221–225 (2019).

[24] Cao, Y. *et al.* Tunable correlated states and spin-polarized phases in twisted bilayer–bilayer graphene. *Nature* **583**, 215–220 (2020).

[25] Shen, C. *et al.* Correlated states in twisted double bilayer graphene. *Nature Phys.* 1–6 (2020).

[26] Polshyn, H. *et al.* Nonvolatile switching of magnetic order by electric fields in an orbital chern insulator. *arXiv:* **2004.11353** (2020).

[27] Chen, S. *et al.* Electrically tunable correlated and topological states in twisted monolayer-bilayer graphene. *arXiv:* **2004.11340** (2020).

[28] Shi, Y. *et al.* Tunable van hove singularities and correlated states in twisted trilayer graphene. *arXiv:* **2004.12414** (2020).

[29] Chittari, B. L., Chen, G., Zhang, Y., Wang, F. & Jung, J. Gate-tunable topological flat bands in trilayer graphene boron-nitride moiré superlattices. *Phys. Rev. Lett.* **122**, 016401 (2019).

[30] Jung, J. & MacDonald, A. H. Accurate tight-binding models for the π bands of bilayer graphene. *Phys. Rev. B* **89**, 035405 (2014).

[31] Varlet, A. *et al.* Fabry-pérot interference in gapped bilayer graphene with broken anti-klein tunneling. *Phys. Rev. Lett.* **113**, 116601 (2014).

[32] McCann, E. & Koshino, M. The electronic properties of bilayer graphene. *Reports on Progress in Physics* **76**, 056503 (2013).

[33] Wimmer, M. *Quantum transport in nanostructures: From computational concepts to spintronics in graphene and magnetic tunnel junctions.* Ph.D. thesis, Universität Regensburg (2008).

[34] Liu, M.-H., Bundesmann, J., Richter, K. *et al.* Spin-dependent klein tunneling in graphene: Role of rashba spin-orbit coupling. *Phys. Rev. B* **85**, 085406 (2012).